

1 Explosive activity on Kīlauea's Lower East Rift Zone fuelled by a volatile-rich, dacitic  
2 melt

3 Penny. E. Wieser\*<sup>1,2</sup>, Marie Edmonds<sup>1</sup>, Cheryl Gansecki<sup>3</sup>, John Maclennan<sup>1</sup>, Frances E. Jenner<sup>4</sup>,  
4 Barbara Kunz<sup>4</sup>, Paula Antoshechkina<sup>5</sup>, Frank Trusdell<sup>6</sup>, R. L. Lee<sup>6</sup>, EIMF<sup>7</sup>.

5 <sup>1</sup>Department of Earth Sciences, University of Cambridge, UK

6 <sup>2</sup>Now at College of Earth, Ocean and Atmospheric sciences, Oregon State University, USA

7 <sup>3</sup>Department of Geology, University of Hawai'i at Hilo, Hilo, HI 96720, USA

8 <sup>4</sup>School of Environment, Earth and Ecosystem Sciences, The Open University, MK7 6AA, UK

9 <sup>5</sup>Division of Geological and Planetary Sciences, California Institute of Technology, Pasadena, CA  
10 91125, USA

11 <sup>6</sup>USGS Hawaiian Volcano Observatory, Hilo, HI 96720, USA

12 <sup>7</sup>Edinburgh Ion Microprobe Facility, School of Geosciences, University of Edinburgh, EH9 3JW, UK

13 Abstract (250 words for G3)

14 Magmas with matrix glass compositions ranging from basalt to dacite erupted from a series of 24  
15 fissures in the first two weeks of the 2018 Lower East Rift Zone (LERZ) eruption of Kīlauea Volcano.  
16 Eruption styles ranged from low spattering and fountaining to strombolian activity. Major element  
17 trajectories in matrix glasses and melt inclusions hosted by olivine, pyroxene and plagioclase are  
18 consistent with variable amounts of fractional crystallization, with incompatible elements (e.g., Cl, F,  
19 H<sub>2</sub>O) becoming enriched by 4-5 times as melt MgO contents evolve from 6 to 0.5 wt%. The high  
20 viscosity and high H<sub>2</sub>O contents (~2 wt%) of the dacitic melts erupting at Fissure 17 account for the  
21 explosive Strombolian behavior exhibited by this fissure, in contrast to the low fountaining and  
22 spattering observed at fissures erupting basaltic to basaltic-andesite melts. Saturation pressures  
23 calculated from melt inclusions CO<sub>2</sub>-H<sub>2</sub>O contents indicate that the magma reservoir(s) supplying  
24 these fissures was located at ~2-3 km depth, which is in agreement with the depth of a dacitic  
25 magma body intercepted during drilling in 2005 (~2.5 km) and a seismically-imaged low Vp/Vs  
26 anomaly (~2 km depth). Nb/Y ratios in erupted products are similar to lavas erupted between 1955-  
27 1960, indicating that melts were stored and underwent variable amounts of crystallization in the  
28 LERZ for >60 years before being remobilized by a dike intrusion in 2018. We demonstrate that  
29 extensive fractional crystallization generates viscous and volatile-rich magma with potential for  
30 hazardous explosive eruptions, which may be lurking undetected at many ocean island volcanoes.

31 Plain Language Summary

32 During the first two weeks of the 2018 eruption of Kīlauea Volcano, Hawai'i, a wide variety of  
33 magma compositions were erupted from 24 separate fissures. Of particular interest is the magma  
34 erupted at Fissure 17, which was much more explosive than nearby fissures, throwing large pieces of  
35 molten rock several hundred metres into the air, causing a serious injury. The explosivity of volcanic  
36 eruptions is partially controlled by the viscosity of the magma (how easily it can flow), and partially  
37 by the amount of dissolved H<sub>2</sub>O and CO<sub>2</sub> (which exsolve like bubbles in a carbonated beverage as the  
38 melt ascends to the surface). We show that melts erupted at Fissure 17 were significantly more

39 viscous and H<sub>2</sub>O-rich than the melts erupted more passively at nearby fissures. These two factors  
40 account for the explosive eruptive style of this fissure. Using the relationship between the amount of  
41 dissolved H<sub>2</sub>O and CO<sub>2</sub> and pressure, we show that erupted magmas were stored at ~2km depth  
42 below the surface since at least 1955-1960 A.D.

### 43 Key points (140 characters)

- 44 1. The first 2 weeks of the 2018 Kīlauea eruption tapped melts undergoing variable amounts of  
45 fractionation at ~2-3 km depth over >60 yrs.
- 46 2. Saturation pressures calculated from melt inclusion volatile contents align with the depth of  
47 a seismically imaged Vp/Vs anomaly.
- 48 3. The strombolian explosions at Fissure 17 result from the high viscosity and the high H<sub>2</sub>O  
49 contents of these dacitic melts

## 50 1. Introduction

51 The main shield-building stage of volcanism at ocean island volcanoes fed by high melt fluxes from  
52 mantle plume melting (e.g., Hawai'i, Galápagos, Réunion) is characterized by the eruption of basaltic  
53 lava flows, spatter, and occasional energetic lava fountains (Macdonald, 1962; Swanson et al., 1979).  
54 On a number of occasions at Kīlauea Volcano, HI, erupted basaltic lava has pooled within existing pit  
55 craters, undergoing extensive fractional crystallization at near atmospheric pressures (e.g., 1959  
56 Kīlauea Iki lava lake, 1963 Alae lava lake, 1965 Makaopuhi Crater; Helz, 1980; Wright et al., 1976). It  
57 is becoming increasingly apparent that andesitic to rhyolitic melts analogous to those formed in  
58 surface lava lakes may also co-exist with basaltic melts at depth within a range of volcanic plumbing  
59 systems, even if these more silicic compositions are poorly represented in erupted rock  
60 compositions (Stock et al., 2020). The first detailed description of such lavas from the shield stage of  
61 a Hawaiian volcano was provided by Bauer et al., (1973), who investigated a rhyodacite from the late  
62 shield stage from the Kaua'ōpu'u ridge of Oahu. In 2005, a hydrothermal injection well on Kīlauea's  
63 Lower East Rift Zone (LERZ) intercepted a stored body of dacitic magma (with a bulk composition of  
64 67 wt% SiO<sub>2</sub>; Teplow et al., 2009). More recently, examination of lava and tephra samples from the  
65 2015 eruption of Wolf Volcano and the 1968 eruption of Fernandina in the Galapagos identified  
66 plagioclase crystals whose compositions indicate that they grew from basaltic trachy-andesite and  
67 trachy-andesitic melts (Stock et al., 2020).

68 In contrast to these tantalizing glimpses of more silicic melts in basalt-dominated ocean island  
69 volcanic settings, the first two weeks of the 2018 Lower East Rift Zone (LERZ) eruption of Kīlauea  
70 Volcano produced significant volumes of lava spanning basaltic to andesitic bulk compositions from  
71 24 different fissures (Fig. 1b, Gansecki et al., 2019). Importantly, while lava lakes act as excellent  
72 natural laboratories to investigate major element evolution of Kīlauea magmas during differentiation,  
73 because the pooling magmas have already degassed the majority of their volatiles, they do not  
74 provide representative insights into volatile element evolution within the plumbing system (Wieser  
75 et al., 2020). The eruption of melts with a wide range of bulk compositions at the surface, combined  
76 with rapid-response sampling of quenched spatter and tephra before it was covered by later lava  
77 flows (Gansecki et al., 2019), provides an unprecedented opportunity to investigate the pre-eruptive  
78 processes producing SiO<sub>2</sub>-rich magmas from ocean island basalts, such as the depth and longevity of  
79 magma storage and differentiation, and the effect of melt composition on eruption style.

80 One fissure, named Fissure 17 (F17) produced highly explosive Strombolian style activity, launching  
81 2-3 m pieces of spatter ~125 m in the air (see  
82 <https://www.youtube.com/watch?v=WXcV6WqvDys&t=108s>; Supporting Video 1). These explosive  
83 outbursts caused a severe injury when spatter was thrown 150 m from the vent and shattered the  
84 leg of a resident on a third floor balcony. F17 also exhibited gas venting and the generation of shock  
85 waves, audible in the town of Mountain View >20 km to the NW. This explosive eruption style at F17  
86 contrasted with the low-moderate fountaining (heights 30 to 80 m) and less energetic spattering  
87 observed at nearby fissures, and even the eastern end of F17 (Fig. 1d-e). F17 is offset ~220 m to the  
88 north-east of the linear trend defined by the other early eruptive fissures (Fig. 1b), and rapid-  
89 response petrological monitoring during the eruption indicated that the western, more explosive  
90 end of F17 was tapping a more SiO<sub>2</sub>-rich composition than the eastern, less explosive end (Gansecki  
91 et al., 2019). However, the cause of the higher explosivity remains uncertain; it has been suggested  
92 that explosivity might result from the involvement of groundwater, or the higher viscosity of these  
93 more SiO<sub>2</sub>-rich melts (Gansecki et al., 2019; Soldati et al., 2021).

94 Here we utilize the major, trace element and volatile element contents of olivine, pyroxene and  
95 plagioclase-hosted melt inclusions to investigate three questions:

- 96 1) What was the cause of the high explosivity observed in the eruptions at the western end of  
97 F17?
- 98 2) What was the most probable parent magma(s) of the variable melt compositions erupted in  
99 the first few weeks of the 2018 eruption?
- 100 3) At what depth were these magmas stored in the LERZ?

101 We show that fissures erupting in the first few weeks of the 2018 eruption tapped a stored magma  
102 body which experienced variable amounts of fractional crystallization at 2-3 km depth. Based on a  
103 comparison of incompatible trace element ratios from 2018 samples and historic activity in this  
104 section of the LERZ, we show that the 2018 eruption tapped a magma body with very similar  
105 chemistry to that supplying the 1955 and 1960 eruption. The large amounts of fractional  
106 crystallization experienced by dacitic melts erupted at F17 drove up melt H<sub>2</sub>O contents to  
107 unprecedented levels at Kīlauea (~2 wt%) which, combined with an increase in melt viscosity,  
108 accounts for the explosive activity observed at this fissure.

### 109 1.1 Chronology of the 2018 LERZ eruption

110 The 2018 LERZ eruption marked the end of a 35-year-long period at Kīlauea Volcano during which  
111 activity was focused predominantly at the Pu'ū'ō'ō vent, on the Middle East Rift Zone (the name  
112 change from Pu'ū'ō'ō signifies that the eruption has ended; Hawai'i Board on Geographic Names).  
113 Following inflation of the summit and Pu'ū'ō'ō during March and April 2018 (Neal et al., 2018;  
114 Patrick et al., 2020), Pu'ū'ō'ō vent collapsed on April 30<sup>th</sup>, accompanied by the propagation of a dike  
115 downrift into the Leilani Estates subdivision on the Lower East Rift Zone (LERZ). Following the  
116 formation of ground cracks, the first eruptive fissures opened on May 3<sup>rd</sup>. Fourteen additional  
117 fissures opened along a linear trend in the first week (F1 to F15; Fig. 1b). These first fissures,  
118 classified as Early Phase 1 by Gansecki et al., (2019), were characterized by whole-rock compositions  
119 with ~4-5 wt% MgO, erupted as relatively small-volume spatter mounds and lava flows. These lavas  
120 are thought to represent material which was intruded during previous eruptive episodes in the  
121 Lower East Rift Zone (e.g., 1790, 1840, 1955 or 1960 A.D; Gansecki et al., 2019; Fig. 1c). The injection  
122 of the dike beneath the Leilani Estates subdivision at the start of May, 2018, is thought to have

123 disturbed these resident melts and forced them to the surface (e.g., by increasing overpressure,  
124 changing the crustal stress state, or thermal rejuvenation).

125 Following an eruptive pause, activity recommenced on May 12<sup>th</sup>-18<sup>th</sup> (termed Late Phase 1), with  
126 more fissures opening up along the same linear trend (Fissures 16, 18, 20, 22). These later fissures  
127 erupted higher magma compositions with higher bulk MgO contents (5-6 wt% vs. 4-5 wt% in Early  
128 Phase 1), which have been interpreted to represent mixing between the early rift-stored component,  
129 and the more MgO-rich magma supplied by the dike (Gansecki et al., 2019). Between the 17-27<sup>th</sup> of  
130 May (Phase 2) effusion rates increased and whole-rock MgO contents increased again to become  
131 very similar to those erupted at Pu'u'ō'ō vent (6-7 wt%), indicating that the vast majority of melts  
132 stored in the LERZ had been flushed from the system (Gansecki et al., 2019; Neal et al., 2018; Patrick  
133 et al., 2019). In addition to this general progression from relatively MgO-poor to MgO-rich melt  
134 compositions, F17 (active 13-25<sup>th</sup> of May, offset to the NE of the other fissures) erupted magma with  
135 significantly lower MgO and higher SiO<sub>2</sub> contents (including andesitic bulk compositions), which is  
136 thought to represent a third, stored magmatic component (Gansecki et al., 2019).

137 By the 28<sup>th</sup> of May (Phase 3), activity had focused at a single fissure (F8, recently renamed  
138 Ahu'ailā'au) which developed a fast-flowing lava channel, and erupted material with even higher  
139 bulk MgO contents resulting from the incorporation of antecrystic olivine crystals (Fig. 2a; Gansecki  
140 et al., 2019; Wieser et al., 2021b). For brevity, to distinguish between this main phase of activity at  
141 Ahu'ailā'au (F8), and the earlier, more MgO-poor material, we refer to activity in early Phase 1, Late  
142 Phase 1 and Phase 2 as "early fissures", and activity at Ahu'ailā'au after May 28<sup>th</sup> as Phase 3.

143 It has been suggested, based on the presence of high forsterite olivines incorporated within Phase 3  
144 lavas, and the bimodal distribution of melt inclusion saturation pressures at 1-2 and 3-5 km, that this  
145 magma originated from the two magma reservoirs identified by geophysical imaging beneath  
146 Kīlauea's summit (Wieser et al., 2021, Lerner et al., 2021), with a hydraulic connection linking these  
147 reservoirs to Ahu'ailā'au (Gansecki et al., 2019; Neal et al., 2018; Patrick et al., 2019). Conversely,  
148 Pietruszka et al. (2021) suggest that major and trace element differences between Phase 3 lavas and  
149 those erupted at Kīlauea's summit and Pu'u'ō'ō prior to the onset of the 2018 eruption rules out a  
150 summit origin, and instead suggest that this MgO-rich magma had accumulated in the Middle East  
151 Rift Zone (MERZ) downrift of Pu'u'ō'ō over ~10 years prior to 2018. The exact source of Phase 3  
152 magma is beyond the scope of this study, which focuses on the early phase lavas erupted between  
153 May 3<sup>rd</sup> to May 16<sup>th</sup>, so we refer to Phase 3 magma as "dike-supplied" to avoid ambiguity.

## 154 2. Methods

### 155 2.1 Analytical methods

156 Spatter, reticulite and lava samples were collected from 9 separate fissures (Fissures 4, 5, 8, 10, 11,  
157 12, 13, 17, and 20) on Kīlauea's LERZ during the 2018 eruption and a follow-up field campaign in  
158 2019 (Supporting Table S1). Care was taken to select the most rapidly-quenched water and air-  
159 quenched material to minimise H<sup>+</sup> diffusion out of melt inclusions (Gaetani et al., 2012). Specifically,  
160 we selected the smallest and most visibly glassy clasts available in each location. Clast size was 0.5-8  
161 cm and water-quenched material was favoured where available. Samples were jaw-crushed, and  
162 olivine, orthopyroxene, clinopyroxene, and plagioclase crystals were picked under a binocular  
163 microscope. Crystals were individually mounted on glass slides using Crystalbond and ground down  
164 to the level of target melt inclusions. Care was taken to prioritize melt inclusions not visibly

165 connected to the outside of the crystal, but particularly in plagioclase-hosted melt inclusions, it was  
166 often difficult to determine the degree of connectivity due to complex melt networks. An indication  
167 of whether each melt inclusion was fully isolated or connected to the carrier melt is provided in  
168 Supporting Dataset S1.

169 All vapour bubbles within melt inclusions were analysed for CO<sub>2</sub> using Raman spectroscopy following  
170 the methods described by Wieser et al., (2021). Unlike the olivine-hosted melt inclusions erupted in  
171 the Phase 3 between 28<sup>th</sup> May and Aug 1<sup>st</sup>, none of the vapour bubbles in melt inclusions from the  
172 early fissures (3<sup>rd</sup>-16<sup>th</sup> May) investigated in this study produced measurable CO<sub>2</sub> peaks, indicating  
173 that the concentration of CO<sub>2</sub> in their vapour bubbles were below the detection limit of Raman  
174 Spectroscopy (~0.02 g/cm<sup>3</sup>; Wieser et al., 2021). Following exposure of a target melt inclusion at the  
175 surface, crystals were mounted in epoxy stubs in groups of 30-40 inclusions, and polished using  
176 progressively finer diamond pastes.

177 Samples were analysed for H<sub>2</sub>O, CO<sub>2</sub>, F (as well as MgO and SiO<sub>2</sub> for normalization) using the Cameca  
178 IMS-7f GEO at the NERC Ion Microprobe Facility at the University of Edinburgh in two analytical  
179 sessions (July 2019, January 2020). A variety of glass standards were analysed with a range of Si  
180 contents to convert counts to element concentrations, and to account for matrix effects on ion  
181 yields as a function of melt SiO<sub>2</sub> content. Detailed analytical information is available in the  
182 Supporting information (Supporting Fig. S1-S2, Supporting Table S2).

183 Following SIMS analysis, the Au coat was removed by polishing on a 1 µm pad (which also helped to  
184 reduce the size of SIMS pits and remove SIMS sputter) and a C coat was applied. Matrix glasses, melt  
185 inclusions, and the composition of the mineral host ~30-100 µm away from each melt inclusion were  
186 analysed using a Cameca SX100 EPMA at the Department of Earth Sciences, University of Cambridge  
187 following the analytical techniques described in Wieser et al., (2021) (also see Supporting Text 1,  
188 Table S3-S9). Care was taken to analyse away from the SIMS pit where possible.

189 Trace elements were measured in melt inclusions and matrix glasses using a Photon Machines G2  
190 193 nm excimer laser system equipped with a HelEx II 2-volume cell coupled to an Agilent 8800 ICP-  
191 MS/MS) at the School of Environment, Earth and Ecosystem Sciences, The Open University.  
192 Depending on the size of the melt inclusion and the number of microlites in matrix glasses, ablation  
193 spots were between 20 and 50 µm. Analyses were conducted following the techniques described by  
194 Jenner et al., (2015) and Wieser et al., (2020). Comparison of measurements of BCR-2G run as  
195 secondary standard to long-term laboratory preferred values is shown in Supporting Dataset S2.

## 196 2.2 Correction for Post-Entrapment Crystallization

197 Olivine-hosted melt inclusions were corrected for the effects of post-entrapment crystallization  
198 (PEC) using the “Olivine MI” tool in Petrolog3.1.1.3 (Danyushevsky and Plechov, 2011), which  
199 requires users to enter the measured major element composition of the melt inclusion, the host Fo  
200 content (both taken from EPMA analyses), and an estimate of the initial FeO<sub>t</sub> content of the melt  
201 inclusion prior to post-entrapment crystallization. The initial FeO<sub>t</sub> content was estimated by  
202 determining a relationship between olivine Fo content and melt FeO<sub>t</sub> contents by calculating the  
203 equilibrium olivine Fo content for co-erupted matrix glasses (see Supporting text 2, Fig. S3). While  
204 olivine-hosted melt inclusions erupted in the later stages of F8 (28<sup>th</sup> May-1<sup>st</sup> Aug) have experienced  
205 up to 35% PEC (Wieser et al., 2021), the maximum amount of PEC experienced by olivines erupted at  
206 the earlier fissures examined in this study is 10% (median= 4%).



207 Unlike for olivine, there is no clear consensus as to the best way to reconstruct orthopyroxene,  
208 clinopyroxene, and plagioclase-hosted melt inclusion compositions for the effects of PEC. We discuss  
209 the approach taken in this study in detail in Supporting Text S2. Briefly, for clinopyroxene we  
210 examine the degree of disequilibrium between each melt inclusion and its host clinopyroxene crystal  
211 using the four equilibrium tests described by Neave et al. (2017):  $K_D^{Fe-Mg}$ , Di-Hd, En-Fs and CaTs.  
212 Melt inclusions lie within the equilibrium field for all parameters except  $K_D^{Fe-Mg}$  (Fig. S4, likely  
213 resulting from the fact that the concentration of FeO and MgO are far more sensitive than other  
214 major elements to the crystallization of small amounts of clinopyroxene on the wall of the melt  
215 inclusion). If a melt inclusion has crystallized clinopyroxene on its walls, the composition of that  
216 clinopyroxene must be added back into the measured melt inclusion composition to restore the  
217 composition at the time of entrapment. Similarly, if the inclusion was heated up and clinopyroxene  
218 dissolved following entrapment, that clinopyroxene must be removed from the measured inclusion  
219 composition. We add/subtract the composition of the host clinopyroxene until the melt inclusion  
220 and host crystal are in  $K_D^{Fe-Mg}$  equilibrium (using Equation 35 of Wood and Blundy, 1997). The  
221 median amount of clinopyroxene addition needed to obtain  $K_D^{Fe-Mg}$  equilibrium was 4 wt% ( $1\sigma=5\%$ ;  
222 Supporting Fig. S5). Corrected melt inclusion compositions meet all four equilibrium tests, and lie  
223 closer to major element trajectories defined by co-erupted matrix glasses than uncorrected  
224 compositions (Supporting Fig. S4-S5).

225 Many orthopyroxene-hosted melt inclusions also lie out of  $K_D^{Fe-Mg}$  equilibrium with the  
226 composition of the host crystal (Supporting Fig. S6). However, unlike for clinopyroxene,  
227 adding/subtracting the composition of the host crystal to reach  $K_D^{Fe-Mg}$  equilibrium results in a  
228 worse fit to the major element trajectories defined by matrix glasses in CaO, and TiO<sub>2</sub> vs. MgO space  
229 (Supporting Fig. S7). Given that most orthopyroxene-hosted melt inclusions lie close to the major  
230 element trajectory of matrix glasses, we leave their compositions uncorrected.

231 The vast majority of plagioclase-hosted melt inclusions lie very close to the compositional trend  
232 defined by matrix glasses, with the exception of 6 melt inclusions erupted at F17, which are offset to  
233 significantly higher FeO (Fig. 2b) and lower CaO contents at ~6 wt% MgO (Supporting Fig. S8). These  
234 offsets are indicative of crystallization of ~15 wt% plagioclase on the walls of the melt inclusion  
235 following entrapment, likely due to extensive cooling between the formation of these relatively high  
236 anorthite crystals (~An<sub>60</sub>) and their incorporation in the significantly cooler F17 melt composition (in  
237 equilibrium with ~An<sub>45-50</sub>). These six melt inclusion compositions were corrected by adding the  
238 composition of the host crystal back into the measured melt inclusion composition to obtain the  
239 best fit to matrix glass data in MgO vs. Al<sub>2</sub>O<sub>3</sub> space (Supporting Fig. S9). All other plagioclase-hosted  
240 melt inclusions were left uncorrected.

## 241 3. Results

### 242 3.1 Major and Volatile Elements

243 The composition of melt inclusions and matrix glasses erupted between May 3<sup>rd</sup> and 16<sup>th</sup> define  
244 coherent trends in major element space, spanning basaltic to dacitic compositions (~7 to 0.5 wt%  
245 MgO, 48 to 68 wt% SiO<sub>2</sub>; Fig. 2a). The compositions of matrix glasses are distinctly clustered, with  
246 the largest group at ~4 wt% MgO (erupted at F4, F5, F8, F10-12 during Early Phase 1 on May 3-9<sup>th</sup>), a  
247 second cluster at ~1 wt% MgO (erupted at F17 on May 14<sup>th</sup>), and a third cluster at ~6-7 wt% MgO  
248 erupted in Phase 3 at Ahu'ailā'au (F8) after May 28<sup>th</sup>. Lavas erupted from F13 following its re-

249 activation (F13-react) plot between the Early Phase 1 and F17 cluster, while lavas erupted at F20 on  
250 May 16<sup>th</sup> plot between the Early Phase 1 cluster and the higher MgO Phase 3 cluster. As above, we  
251 refer to early Phase 1 fissures (F4, F5, F8, F10-12), F13-react, F17 and F20 as early fissures (3<sup>rd</sup>-16<sup>th</sup>  
252 May) to distinguish them from the more MgO-rich material erupted at Ahu'ailā'au (F8) after May  
253 28<sup>th</sup> in Phase 3.

254 Melt inclusion and matrix glass Cl and F concentrations increase with decreasing melt MgO contents,  
255 with the most volatile-rich dacitic melt inclusions erupted at F17 having Cl and F concentrations of  
256 ~1000 ppm (3-5 times higher than observed in melt inclusions erupted in phase 3; Fig. 3a-b). F  
257 concentrations show significantly more scatter than Cl concentrations. The upper limit of melt  
258 inclusion H<sub>2</sub>O contents also increases with fractional crystallization, reaching 1 wt% in the early  
259 Phase 1 lavas with ~4 wt% MgO, and up to 2 wt% in melt inclusions erupted at F17 with 0.5-1 wt%  
260 MgO (Fig. 3d). These F17 measurements greatly exceed the highest H<sub>2</sub>O content measured in melt  
261 inclusions from historic eruptions at Kīlauea (~1 wt% H<sub>2</sub>O, Sides et al., 2014b). Unlike Cl, F, H<sub>2</sub>O and  
262 Zr (Fig. 2d, Fig. 3a-c), melt inclusion CO<sub>2</sub> concentrations are approximately constant between 4 and  
263 6 wt% MgO (with a maximum concentration of ~300-400 ppm), then decline slightly with decreasing  
264 MgO to ~200 ppm at 0.5-1 wt% MgO (Fig. 3c).

### 265 3.2 Trace elements

266 As discussed further in section 4.4, Nb/Y is not extensively fractionated during crystallization at  
267 Kīlauea, so can be used to identify distinct magma batches (Pietruszka et al., 2021). Early Phase 1  
268 matrix glasses from F4, F5, F8, F10-12 (green symbols) have Nb/Y ratios of ~0.6-0.8, which overlap  
269 with the composition of matrix glasses erupted at F17 (Fig. 4a). In contrast, matrix glasses erupted at  
270 F13 following its reactivation and F20 have lower Nb/Y ratios, plotting closer to the composition of  
271 Phase 3 glasses. Overall, the trends defined by matrix glasses measured by LA-ICP-MS in this study  
272 are very similar to those determined by whole-rock XRF measurements (Pietruszka et al., 2021,  
273 magenta dots, Fig. 4a).

274 Unlike the temporal variations seen in matrix glass and whole-rock trace element compositions,  
275 there are no apparent inter-sample differences in the Nb/Y ratios of melt inclusions erupted from  
276 early fissures, or relationships between Nb/Y ratios and host crystal An# or Mg# in these samples  
277 (Fig. 4c-d). As for matrix glasses, the vast majority of melt inclusions from Phase 3 (orange colors;  
278 Fig. 4c-d) lie to distinctly lower Nb/Y ratios, with only a small number of melt inclusions erupted on  
279 May 28<sup>th</sup> overlapping with the Nb/Y ratios of melt inclusions from early fissures (particularly those  
280 hosted in lower forsterite olivines).

## 281 4. Discussion

### 282 4.1 Modelling Fractional Crystallization

283 The coherent trends in major and volatile element trajectories defined by melt inclusions and matrix  
284 glasses indicate that the dominant cause of chemical variability in erupted melts during the first two  
285 weeks of the 2018 eruption was fractional crystallization. Previous studies have shown that Kīlauea  
286 melts fractionate only olivine (+minor Cr-spinel) at >6.8 wt% MgO, defining a relatively flat trajectory  
287 for all elements vs. MgO (Wright and Fiske, 1971). Next, clinopyroxene joins the liquidus, followed by  
288 plagioclase after only 5-15 °C cooling, as well as minor orthopyroxene (Helz and Wright, 1992). The  
289 crystallization of plagioclase accounts for the rapid increase in melt FeO<sub>T</sub> as MgO contents drop from  
290 6 to 4 wt% (Fig. 2b). The appearance of plagioclase and clinopyroxene on the liquidus also causes the

291 slope of relatively incompatible elements like  $\text{TiO}_2$  and Zr vs. MgO to greatly increase, because a  
292 larger mass of solid is fractionated for a given decrease in melt MgO content. At  $\sim 4$  wt% MgO, Fe-Ti  
293 oxides saturate (Helz and Wright, 1992), driving the concentration of  $\text{FeO}_T$  and  $\text{TiO}_2$  down, and  $\text{SiO}_2$   
294 up. Concurrently, P/Nd begins to decline (along with  $\text{P}_2\text{O}_5$ ; Supporting Fig. S10), indicating the onset  
295 of apatite crystallization (visible as microphenocrysts in matrix glasses from F17).

296 Fractional crystallization models were run using alphaMELTS for MATLAB (Rhyolite melts V1.2.0,  
297 Antoshechkina and Ghiorso, 2018; Ghiorso and Gualda, 2015; Gualda et al., 2012) to recreate  
298 observed major element trends. Although it is likely that the melt fractionating within the LERZ was  
299 a previously stored component, the starting composition of models was set as the average major-  
300 element composition of glasses erupted in Phase 3. This is because the vast majority of literature  
301 data for previous eruptions comprises whole-rock compositions, which may be affected by crystal  
302 addition. The starting composition used for the modelling lies within the range of whole-rock  
303 compositions from various early fissures from Gansecki et al. (2019), justifying this choice. The initial  
304  $\text{Fe}^{3+}/\text{Fe}_T$  ratio was set at 0.15 (Lerner et al., 2021; Moussallam et al., 2016), and models were run  
305 without a buffer, allowing for changes in oxidation state following Fe-Ti oxide saturation. The  
306 pressure was set at 650 bars, based on the upper range of saturation pressures measured in Early  
307 Phase 1 melt inclusions (see section 4.5). The trajectory of trace and volatile elements during  
308 fractional crystallization was modelled using the mass of solid phases produced, and the fractional  
309 crystallization equation ( $C_{\text{final}}=C_{\text{initial}}*F^{D-1}$ , where F is the amount of melt remaining, and D is the bulk  
310 partition coefficient).

311 In detail, we consider two separate model trajectories in MELTS. Model A (red line) was run with an  
312 initial  $\text{H}_2\text{O}$  concentration of 0.1 wt%. Model A is a good match to the trajectory of major elements  
313 from  $\sim 6.8$  to 4 wt% MgO, capturing the sharp increase in  $\text{FeO}_T$  and  $\text{TiO}_2$  contents with decreasing  
314 MgO. At lower MgO contents, Model A is a good fit to  $\text{FeO}_T$ ,  $\text{TiO}_2$  and  $\text{SiO}_2$  (Fig. 2a-c) but  
315 overestimates CaO, and underestimates  $\text{Al}_2\text{O}_3$  (Supporting Fig. S11) indicating that the ratio of  
316 clinopyroxene vs. plagioclase fractionating in this model is incorrect. Similarly, Model A does not  
317 recreate the prominent downtick in  $\text{P}_2\text{O}_5$  (and P/Nd) caused by apatite crystallization, because  
318 MELTS currently only accounts for a hydroxy-apatite phase (rather than the more stable fluorapatite  
319 observed in natural magmas; Rooney et al., 2012). The failure to correctly model apatite saturation  
320 may also account for some of the overestimation of melt CaO contents at  $<4$  wt% MgO (Supporting  
321 Fig. S11). However, despite these major-element discrepancies, the concentration of Zr and Cl  
322 (assuming complete incompatibility) in Model A provides a good fit to the composition of melt  
323 inclusions and matrix glasses. This indicates that MELTS model results are accurately predicting the  
324 amount of solid being fractionated, even if predictions of relative phase proportions are slightly  
325 inaccurate.

326 If MELTS models are initialized with water contents similar to those in melt inclusions with  $\sim 6$  wt%  
327 MgO ( $\text{H}_2\text{O}_i=0.5$  wt%, Model B, Fig. 2, dashed black lines), MELTS saturates Fe-Ti oxides significantly  
328 earlier and plagioclase later than Model A, such that Model B fails to achieve the prominent  $\text{TiO}_2$  and  
329 FeO enrichment seen in erupted glass compositions. This has been noted previously for Kīlauea by  
330 Garcia (2003). Fortunately, the total mass of solids predicted by model A and model B are reasonably  
331 similar, so these models predict similar trajectories for incompatible elements such as Zr (Fig. 2d).  
332 We also generate a 3<sup>rd</sup> major element path for fractional crystallization, using MELTS model A at  $>4$   
333 wt% MgO, and a best fit through measured glass and melt inclusion data for  $<4$  wt% (Supporting Fig.  
334 S11). The major element differences between these three models have a relatively small effect on



335 volatile solubility (Supporting Fig. S12) and calculations of melt viscosity (Fig. 5b). This justifies the  
336 use of Model B to investigate changes in volatile systematics and viscosity during fractional  
337 crystallization, even though this model doesn't fully recreate the observed major element  
338 systematics (Fig. 2).

339 Rhyolite-MELTS V1.2.0 fails to reproduce olivine-only fractionation at >6.8 wt% MgO, so this section  
340 of the fractionation path was modelled using the "reverse crystallization" (RFC) tool in Petrolog3  
341 (Danyushevsky and Plechov, 2011) from the specified starting composition.

#### 342 4.2 Volatile Element Evolution during Crystallization

343 MELTS modelling demonstrates that the prominent enrichment in melt inclusion Cl concentrations  
344 with decreasing MgO results from extensive fractional crystallization (Fig. 3a). F data shows  
345 significantly more scatter than Cl (Fig. 3b), but approximately follows the fractional crystallization  
346 trend. Notably, six plagioclase-hosted F17 melt inclusions with higher MgO contents (~4-6 wt%) lie  
347 significantly above the fractional crystallization line for F, indicating that these inclusions may have  
348 diffusively re-equilibrated with the significantly more F-rich carrier melts in which they were erupted  
349 (Fig. 3b). Apparent open-system behavior of F in olivine-hosted melt inclusions has been noted  
350 previously by Koleszar et al., (2009) and Portnyagin et al. (2008), while Neave et al. (2017) attribute F  
351 enrichment in plagioclase-hosted melt inclusions to diffusive pile up during rapid growth. We favour  
352 diffusive re-equilibration here, because many F17 melt inclusions have lower F contents than co-  
353 erupted matrix glasses, and it is only the most MgO-rich melt inclusions which are expected to have  
354 equilibrated with more F-rich, MgO-poor melts that show notable enrichment above the fractional  
355 crystallization trend. Two of these melt inclusions also show elevated H<sub>2</sub>O contents (Fig. 3d), which is  
356 consistent with these more primitive melt inclusions equilibrating with the more MgO-poor, F- and  
357 H<sub>2</sub>O- rich F17 carrier melt prior to eruption (with F re-equilibration appearing to occur faster than  
358 H<sub>2</sub>O re-equilibration in plagioclase).

359 Accounting for these complexities with F, the relative similarity of the trajectories of matrix glasses  
360 and melt inclusions indicates that the amount of F and Cl degassed upon eruption is sufficiently  
361 small that it cannot be resolved petrologically by comparing melt inclusions and matrix glasses. In  
362 contrast, H<sub>2</sub>O and CO<sub>2</sub> degas strongly upon eruption, shown by the significantly lower concentrations  
363 in matrix glasses relative to melt inclusions (Fig. 3c-d).

364 The upper limit of melt inclusion H<sub>2</sub>O contents is bracketed by treating H<sub>2</sub>O as an incompatible  
365 element in MELTS model A, with a number of melt inclusions plotting to lower H<sub>2</sub>O contents. In  
366 contrast, melt inclusion CO<sub>2</sub> contents show a slight decline with decreasing MgO contents, again  
367 with a lot of scatter. The evolution of H<sub>2</sub>O-CO<sub>2</sub> is significantly more complicated than elements like Zr  
368 and Cl, because Kīlauea melts are saturated in a mixed H<sub>2</sub>O-CO<sub>2</sub> fluid at crustal pressures (Gerlach et  
369 al., 2002). This means there is a competing influence between their incompatible behavior in solid  
370 phases and their loss to an exsolving fluid phase. To demonstrate this trade-off, we use the solubility  
371 model MagmaSat (Ghiorso and Gualda, 2015) implemented in the Python3 tool VESICAL (Iacovino et  
372 al. 2021) to calculate the solubility of pure-CO<sub>2</sub> fluids and pure-H<sub>2</sub>O fluids at 650 bars for the  
373 synthetic major element path which provides the best fit to measured glass and melt inclusion data  
374 (Supporting Fig. S11), using temperatures from the MgO geothermometer of Helz and Thornber,  
375 (1987). At low pressures where non-ideality between H<sub>2</sub>O-CO<sub>2</sub> is negligible, the concentration of  
376 either volatile species will not exceed the pure solubility limit. The solubility of pure CO<sub>2</sub> is relatively  
377 low (~400 ppm), and plots close to the measured CO<sub>2</sub> contents of melt inclusions (dashed blue line,

378 Fig. 3c). In contrast, the solubility of pure H<sub>2</sub>O is much higher, plotting significantly above the  
379 concentration of melt inclusions (dashed blue line, Fig. 3d).

380 In reality, H<sub>2</sub>O-CO<sub>2</sub> exsolves as a mixed fluid in magmatic systems. At the low pressures considered  
381 here, where mixing between H<sub>2</sub>O and CO<sub>2</sub> is close to ideal, the behavior of mixed fluids is best  
382 understood considering Henry's Law (Lowenstern, 2001). Namely, the addition of H<sub>2</sub>O to a pure CO<sub>2</sub>  
383 fluid lowers the partial pressure of CO<sub>2</sub>, and therefore lowers its solubility in the co-existing melt  
384 phase. Similarly, adding CO<sub>2</sub> to a pure H<sub>2</sub>O fluid lowers the solubility of H<sub>2</sub>O in the melt. The solubility  
385 of H<sub>2</sub>O-CO<sub>2</sub> in equilibrium with a mixed fluid during fractionation can be simulated in alphaMELTS for  
386 MATLAB along the fractionation path of MELTS model B (which has realistic initial H<sub>2</sub>O contents).  
387 From 6 to 4 wt% MgO, when the melt is relatively H<sub>2</sub>O -poor, the composition of the exsolved vapour  
388 phase ( $X_{\text{CO}_2}$ ) is >90 wt% CO<sub>2</sub>. With increasing fractionation, the progressive rise in the H<sub>2</sub>O content of  
389 the melt causes  $X_{\text{CO}_2}$  to steadily decrease, reaching ~65 wt% (40 mol%) at 0.5 wt% MgO (Fig. 5a). This  
390 decrease in the proportion of CO<sub>2</sub> in the fluid causes the CO<sub>2</sub> solubility predicted by MELTS model B  
391 (black dotted line, Fig. 3c) to decrease more rapidly than the model for pure CO<sub>2</sub> solubility. MELTS  
392 model B tracking mixed volatile solubility during fractional crystallization effectively brackets the  
393 upper limit of the majority of melt inclusion data, providing strong evidence that melts were vapour-  
394 saturated at depth, and that the solubility model MagmaSat used in Rhyolite-MELTS is effectively  
395 capturing changes in volatile solubility during fractional crystallization.

396 A significant proportion of the total amount of CO<sub>2</sub> in the system is lost to the vapour phase during  
397 fractional crystallization, partially because  $X_{\text{CO}_2}$ >65 wt% across most of the fractionation interval, and  
398 because there was so little CO<sub>2</sub> in the system to start with (~385 ppm at 6.7 wt% MgO). For example,  
399 fractionation of just 0.02 wt% fluid with  $X_{\text{CO}_2}$ =80 wt% removes 160 ppm of CO<sub>2</sub> from the system. In  
400 contrast, the higher initial mass of H<sub>2</sub>O in the system combined with high  $X_{\text{CO}_2}$  ratios mean that very  
401 little H<sub>2</sub>O is lost to the fluid; in the example above only 40 ppm of H<sub>2</sub>O is lost to the vapour compared  
402 to 160 ppm of CO<sub>2</sub>. Notably, this is only ~1% of the initial amount of H<sub>2</sub>O in the system, which is well  
403 within analytical error of SIMS measurements (Fig. 5b). Thus, the trajectory of melt H<sub>2</sub>O during  
404 extensive fractional crystallization at shallow crustal pressures in the presence of an exsolved H<sub>2</sub>O-  
405 CO<sub>2</sub> fluid is very similar to models of H<sub>2</sub>O enrichment assuming no volatile loss. Minimal H<sub>2</sub>O-loss to  
406 the exsolving fluid accounts for the high H<sub>2</sub>O contents of the dacitic melts erupted at F17. We  
407 caution that the apparent incompatible behavior of H<sub>2</sub>O should not be interpreted as evidence for  
408 "H<sub>2</sub>O-undersaturation"; it may simply indicate that the magma was saturated in a mixed fluid that  
409 was relatively H<sub>2</sub>O-poor.

410 While the upper limit of melt inclusion volatile contents follow MELTS model B, a number of melt  
411 inclusions plot to lower CO<sub>2</sub> and H<sub>2</sub>O concentrations. The cause of this spread is best evaluated using  
412 plots of H<sub>2</sub>O vs. CO<sub>2</sub>, with degassing paths for specific melt inclusions overlain (calculated using the  
413 solubility model MagmaSat implemented in VESIcal; Ghiorso and Gualda, 2015; Iacovino et al., 2021;  
414 Fig. 6). Some samples (e.g., F10; Fig. 6b) show tightly clustered volatile contents, which plot very  
415 close to fractional crystallization trends (Fig. 3c-d). Others (e.g. F13-react, Fig. 6a) show considerable  
416 spread to lower CO<sub>2</sub> contents, approximately following the trajectory of modelled degassing paths.  
417 This indicates that many melt inclusions were formed or sealed during ascent, trapping a  
418 progressively degassing magma. Horizontal spread to variable H<sub>2</sub>O contents may reflect diffusive re-  
419 equilibration of melt inclusions with degassing carrier melts, or crystals being entrained into melts  
420 with higher H<sub>2</sub>O than those they grew from (e.g., 6 plag-hosted MI from F17). F17 melt inclusions  
421 show the most scatter, which can be recreated by a combination of the trajectory shown by MELTS

422 model B, degassing, and H<sup>+</sup> re-equilibrium (Fig. 6d). However, without measurements of D/H ratios  
423 in melt inclusions, the exact contribution of degassing, fractional crystallization, and re-equilibration  
424 of H<sub>2</sub>O is difficult to determine. In general, we note that H<sup>+</sup> loss through plagioclase is likely slower  
425 than in olivine (Johnson and Rossman, 2013). Additionally, we observe that multiple melt inclusions  
426 hosted within single crystals erupted at F17 have a wide range of H<sub>2</sub>O-CO<sub>2</sub> contents, and there is no  
427 relationship between H<sub>2</sub>O contents and the position of the melt inclusion within the crystal, or the  
428 size of the inclusion (inconsistent with H-loss by diffusion, Supporting Fig. S13-15). The observed  
429 variability within individual crystals is more consistent with melt inclusions being trapped at various  
430 points along a degassing path. The influence of degassing is considered further in section 4.5.

### 431 4.3 Implications for Eruption Style Variations

432 The higher water contents of F17 melts relative to basaltic and basaltic-andesite melts (resulting  
433 from larger amounts of fractional crystallization) means that a significantly larger volume of volatiles  
434 is exsolved as these melts ascend to the surface (Fig. 7c). We demonstrate this by tracking the ascent  
435 of magma along a closed-system degassing path in alphaMELTS for MATLAB for a composition  
436 representative of the basaltic material erupted at the early fissures (MgO=4.3 wt%, SiO<sub>2</sub>=50.8 wt%,  
437 H<sub>2</sub>O=0.95 wt%) and a composition representative of the dacitic melt erupted at F17 (MgO=1 wt%,  
438 H<sub>2</sub>O=1.78 wt%; Fig. 7). For both melt compositions, these models predict that the volume of  
439 exsolved volatiles relative to the total volume of the system (fluid+melt+crystals) is very low at 650  
440 to 400 bars (Fig. 7a), and degassing only produces measurable changes in the dissolved  
441 concentration of CO<sub>2</sub> in the melt (Fig. 7b). This is also shown on the degassing paths in Fig. 6a-d. At  
442 <300 bars for the dacitic melt, H<sub>2</sub>O begins to exsolve in larger quantities, causing the volume of  
443 exsolved volatiles to increase rapidly with decreasing pressure. The onset of significant quantities of  
444 H<sub>2</sub>O exsolution occurs at a pressure ~100-200 bars lower for basaltic melts compared to dacitic melt.

445 To compare these ascent paths, we divide the volume of volatiles exsolved during ascent of the  
446 dacite by the volume of volatiles exsolved during ascent of the basaltic (Fig. 7a). The higher initial  
447 H<sub>2</sub>O content of the dacite, combined with the fact that H<sub>2</sub>O begins to exsolve at higher pressures  
448 means that at ~200 bars, the volume of volatiles in the dacitic melt is nine times higher than in the  
449 basaltic melt (Fig. 7c). The larger volatile volume at depth, combined with higher melt viscosity, will  
450 promote bubble nucleation and coalescence, which is a key driver of Strombolian activity (Jaupart  
451 and Vergnolle, 1988). By the time these melts reach the surface, where almost all of the initial H<sub>2</sub>O  
452 in both melts has exsolved, the volume of volatiles exsolved in the dacitic melt is approximately  
453 twice that for the rift-stored basalts.

454 Eruption style is also influenced by melt viscosity. First, we model changes in melt viscosity during  
455 fractional crystallization (Fig. 5c), and then assess changes in viscosity during ascent using the  
456 viscosity model of Giordano et al. (2008) (Fig. 7d). As viscosity is highly sensitive to melt H<sub>2</sub>O content,  
457 we calculate viscosity for the major and volatile-element trajectories from MELTS Model B, using  
458 MELTS temperatures and temperatures from Helz and Thornber (1987). Because Model B is a  
459 relatively poor fit to major element data at <4 wt% MgO, we also calculate the viscosity for the best  
460 fit to measured major and volatile element data (see Supporting Fig. S11) using the MgO  
461 geothermometer of Helz and Thornber, (1987) for melt temperature, and H<sub>2</sub>O contents from a best  
462 fit to MELTS model B. The two viscosity models using Helz and Thornber (1987) are very similar,  
463 predicting a rapid increase in melt viscosity below 4 wt% MgO (Fig. 5b) as a result of SiO<sub>2</sub> enrichment  
464 in the melt following the onset of Fe-Ti oxide fractionation (Fig. 2a) and a steady decline in the  
465 temperature of the melt. The model using MELTS temperatures is similar until ~2 wt% MgO, after

466 which it rises to higher values because MELTS predicts significantly lower temperatures than Helz  
467 and Thornber (1987).

468 Prior to the onset of degassing upon ascent, the dacitic melt is ~10-20 times more viscous than the  
469 basaltic melt (Fig. 7d). During ascent along a closed-system degassing path, the discrepancies in  
470 viscosity between the basaltic and dacitic melt are enhanced, so at the surface, the dacitic melt is  
471 70-130 times more viscous (Fig. 7d, Soldati and Dingwell, 2021). The relative viscosities calculated in  
472 our models are very similar to viscosities obtained from direct measurements of 2018 lavas at  
473 atmospheric pressure (yellow and blue stars on Fig. 7d, Soldati and Dingwell, 2021) particularly when  
474 the Helz and Thornber, (1987) MgO thermometer is used for both comparisons. The increasing  
475 contrast in viscosity between the basalt and dacite during ascent to the surface results from the fact  
476 that the dacitic melt has more H<sub>2</sub>O to lose (which drives a rapid increase in viscosity). It is also worth  
477 noting that these calculations only track the viscosity of the melt phase. While the proportion of  
478 crystals relative to melt is similar for F17 vs. early phase 1 lavas (~39% vs. 42%; Gansecki et al.,  
479 2019), F17 samples have completely different crystal shapes, with a larger number of smaller,  
480 elongated plagioclase crystals which may further amplify these differences in viscosity (see BSE  
481 images in Supplement Dataset S3, p78-80 vs. p82-84). The larger volume of bubbles in F17 melts will  
482 also affect viscosity, although this is difficult to quantify because it depends greatly on the amount of  
483 shear rate and strain of bubbles (Llewellyn et al., 2002; Manga and Loewenberg, 2001).

484 It is well recognised that differences between Hawaiian style lava fountaining (exhibited weakly by  
485 the early fissures) and Strombolian activity (exhibited strongly by the F17 andesite) are controlled by  
486 magma rise speed, viscosity, and volatile content (Houghton et al., 2016; Houghton and  
487 Gonnermann, 2008; Wilson and Head, 1981). Strombolian eruptions occur when bubbles can  
488 coalesce and rise faster than the surrounding melt, resulting in the bursting of large bubbles at the  
489 surface along with relatively minimal volumes of melt (see Supporting Video 1 and 2, Wilson and  
490 Head, 1981). Separated two phase flow is promoted at higher gas/magma ratios and for higher melt  
491 viscosities, which tends to reduce magma rise rates (Gonnermann and Manga, 2013). The 10-100  
492 higher viscosities of F17 melts compared to more primitive basaltic melts at <300 bars (Fig. 7d),  
493 combined with the higher exsolved volatile fraction (Fig. 7c), mean that melt rise speeds would have  
494 been significantly slower for a given conduit width and pressure gradient, favouring bubble rise and  
495 coalescence (e.g., Parfitt and Wilson, 1995). Thus, the high explosivity observed at F17 is likely a  
496 direct consequence of extensive fractional crystallization driving up melt viscosity and H<sub>2</sub>O contents,  
497 causing a larger volume of bubbles to exsolve (and coalesce) at greater depths in the conduit at a  
498 deeper depth, along with likely feedbacks between a higher viscosity and lower ascent rates in the  
499 dacitic melt (further favouring bubble coalescence).

#### 500 4.4 Identifying Parental Magmas

501 Major and volatile element systematics indicate that melts erupted in the first two weeks of the  
502 2018 eruption underwent extensive (and variable amounts) of fractional crystallization during rift-  
503 zone storage. However, using major elements systematics alone it is difficult to determine whether  
504 these melts were derived from fractionation of a single parent magma, or a number of different  
505 magma bodies, because the major element contents of different Kīlauea eruptions are relatively  
506 similar at a given MgO content (Helz and Wright, 1992). In contrast, through time, Kīlauea eruptions  
507 show clear variations in incompatible trace element ratios such as Nb/Y, La/Yb, and Zr/Y (Fig. 4b),  
508 interpreted to represent heterogeneity in the Hawaiian mantle plume, as well as variations in the  
509 degree of mantle melting (Pietruszka and Garcia, 1999a, 1999b). It is probable that the parent

510 magma(s) for the variably-evolved melts erupted in 2018 were intruded into the rift zone and  
511 erupted at the surface during a previous eruptive episode (the most recent eruptive events occurred  
512 in 1790, 1823, 1840, 1955 and 1960 A.D). The 1790 and early 1955 fissures are of particular interest,  
513 because these fissures were located in the same area of the LERZ as the 2018 eruption (Fig. 1c; Helz,  
514 2008; Moore, 1992; Wright and Fiske, 1971). Similarly, the 1960 eruption occurred a short distance  
515 downrift, so presumably its magma supply passed through the section of the rift zone where the 2018  
516 eruption occurred. Here, we use trace element ratios to determine the composition of historic  
517 eruptions on the LERZ and compare these to our measurements from 2018 eruptive products to  
518 deduce the most probable parent magma(s).

519 Unlike previous work using trace elements to track magma batches at Kīlauea in lavas which have  
520 undergone mostly olivine-saturation (Pietruszka and Garcia, 1999b; Wieser et al., 2019), the melts  
521 analysed here have experienced fractionation of a number of phases (olivine, clinopyroxene,  
522 orthopyroxene, plagioclase,  $\pm$  ilmenite, magnetite, and apatite). The presence of these other phases  
523 in addition to olivine provides a potential mechanism for these trace element ratios to be  
524 fractionated during crystallization, which might obscure attempts to compare rift-stored melt  
525 compositions to magma batches defined by analyses in the literature of mostly olivine-saturated  
526 samples from previous LERZ eruptions and Kīlauea's summit. To assess which element ratios are  
527 least fractionated by extensive crystallization at Kīlauea, we use the trace element systematics of  
528 glasses from drill cores taken through the Kīlauea Iki lava lake (Greaney et al., 2017). This lava lake  
529 experienced extensive fractionation of a single magma batch across a range of MgO contents very  
530 similar to the lavas examined here, with a very similar mineral assemblage (Helz, 1980; Helz and  
531 Thornber, 1987). Thus, evaluation of changes in trace element contents with decreasing MgO in  
532 these lava lake samples providing a unique opportunity to establish whether trace element ratios  
533 are fractionated across this differentiation interval. Between 6 and  $\sim$ 0 wt% MgO, Kīlauea Iki matrix  
534 glass Nb, Yb and Y all increase by a factor of 2-3, while La and Zr behave more incompatibly;  
535 increasing by a factor of 3-4 times (Supporting Fig. S16). This causes the Nb/Y ratio to remain almost  
536 constant during extensive fractionation, while La/Yb increases slightly ( $\sim$ 20%), and Zr/Y more than  
537 doubles (Supporting Fig. S17). Pietruszka et al., (2021) also demonstrate that Nb/Y is resistant to  
538 fractionation using available partitioning data for relevant phases. In addition to being the least  
539 fractionated ratio, it is also advantageous to use Nb/Y for comparisons because it is the only trace  
540 element ratio which has been reported by a number of different studies investigating historic lavas  
541 on the LERZ (because both Nb and Y can be measured accurately and precisely by XRF, unlike La and  
542 Yb).

543 Previous work has shown that Nb/Y ratios in historic summit and rift eruptions follow a prominent  
544 trough-peak-trough shape between 1800 to present (Garcia et al., 2021; Marske, 2010; Pietruszka  
545 and Garcia, 1999b, 1999a). The highest Nb/Y ratios are observed in lavas from the mid 1900s,  
546 declining towards the values measured during the final stages of the Pu'ū'ō'ō eruption (Fig. 4b;  
547 Gansecki et al., 2019). Nb/Y ratios from whole rock analyses of previous LERZ eruptions follow a  
548 similar trend to summit eruptions (Helz and Wright, 1992; Marske, 2010; Norman, 2005). Matrix  
549 glasses erupted in Early Phase 1 in 2018 have much more similar Nb/Y ratios to the 1955-1960  
550 eruptions than melts erupted in the period between 1790-1840 AD (characterized by lower Nb/Y  
551 ratios;  $\sim$ 0.5-0.6, see also Pietruszka et al., 2021). This indicates that melts erupted in 1955 or 1960  
552 are a more probable parent than those erupted in 1790 and 1840.



553 Two main phases of the 1955 eruption have been identified, with an early phase (1955E) thought to  
554 tap more MgO-poor magmas already present within the rift zone (5-5.7 wt % MgO<sub>Whole-rock</sub>), while  
555 later phase (1955L) tapped more MgO-rich magmas (6.2-6.8 wt% MgO<sub>Whole-rock</sub>) interpreted to reflect  
556 mixing of the 1955E lava with a more MgO-rich, summit-derived component (Helz and Wright,  
557 1992). This is analogous to the temporal evolution from MgO-poor to MgO-rich observed in the 2018  
558 eruption. Using the analyses of Marske (2010), along with additional analyses of 1955 lavas from  
559 Helz and Wright, (1992) and Norman, (2005), we show that the mean and range of Nb/Y ratios in  
560 lavas erupted in the early and late phase of 1955 are a good match to the matrix glass compositions  
561 erupted in Early Phase 1 in 2018 (Fig. 4a). Using Nb/Y ratios alone, it is not possible to definitively  
562 distinguish between the 1955E, 1955L and 1960 lavas, but it is notable that the 1955E vents are  
563 geographically extremely close to the 2018 vents (Fig. 1c).

564 Whole-rock Nb/Y ratios (pink dots on Fig. 4a, Pietruszka et al., 2021) of lavas erupted in the first 20  
565 days of the 2018 eruption form a mixing trend between the “1955-1960 like” Nb/Y ratios exhibited  
566 by Early Phase 1 lavas, and the Nb/Y ratios measured in Phase 3. This trend is also seen in our matrix  
567 glass analyses of F13-react and F20. These mixing trends indicate that LERZ-stored melts were  
568 progressively flushed out by the more MgO-rich, lower Nb/Y component supplying phase 3  
569 (Gansecki et al., 2019). Interestingly, while some of the more MgO-rich samples erupted at F17 (WR  
570 MgO=3-4 wt%, Gansecki et al., 2019; Pietruszka et al., 2021) show evidence for mixing with the  
571 lower Nb/Y component from Phase 3 (glass MgO=~0.5 wt%, WR MgO=2.3-2.6 wt%, Supporting Fig.  
572 S18), our sample has glass Nb/Y ratios which entirely overlap with these Early Phase 1 glasses (Fig.  
573 4a). This overlap indicates that melts erupted in Early Phase 1 and at F17 were likely derived from a  
574 common parent magma, and that our F17 sample experienced minimal mixing with magma erupted  
575 in Phase 3. Thus, it seems likely that the initial activity at F17 was triggered by an increase in  
576 overpressure, change in crustal stress, or thermal rejuvenation resulting from the intrusion of a dike  
577 containing Phase 3 magma into this section of the rift zone, rather than as a direct consequence of  
578 mixing between different magma compositions. Subsequent mixing of magmas indicated by whole-  
579 rock Nb/Y data from Gansecki et al., (2019) and Pietruszka et al., (2021; Supporting Fig. S18) likely  
580 helped to liberate more of this stored material, fuelling the large lava flows with more MgO-rich  
581 compositions that erupted from F17 until May 25<sup>th</sup> (not sampled in this study).

582 Melt inclusion Nb/Y ratios in plagioclase crystals show no correlation with the anorthite (An) content  
583 of the host (Fig. 4c), which is consistent with a common parental magma for all rift-stored melts.  
584 Similarly, melt inclusion Nb/Y ratios in olivine, clinopyroxene and orthopyroxene from early fissures  
585 show no correlation with host Mg# [Mg/(Mg+Fe) atomic; Fig. 4d], and are clearly distinct from the  
586 significantly lower Nb/Y ratios in matrix glasses and the majority of melt inclusions in Phase 3. This  
587 indicates that very few inclusions trapped melts that had undergone significant mixing with Phase 3  
588 melts. Interestingly, 3 plagioclase-hosted melt inclusions from early F8, F5 and F20 plot with F17  
589 melt inclusions in Nb/Y-An space, and 6 inclusions from F17 have higher MgO contents and major  
590 element contents indicating post-entrapment cooling. This supports the idea that more MgO-poor  
591 pockets of melt exist in close proximity with more MgO-rich bodies in the rift zone magma body, in  
592 order for more MgO-rich fissures to scavenge more An-poor crystals, and for more MgO-poor  
593 fissures to scavenge more An-rich crystals. The five olivine-hosted melt inclusions erupted on May  
594 28<sup>th</sup> in Phase 3 (F8) with higher Nb/Y ratios (~0.7; Fig. 4d) are hosted in olivines with some of the  
595 lowest forsterite contents of phase 3, and have melt inclusion TiO<sub>2</sub> contents overlapping with Early  
596 Phase 1 melt inclusions and glasses (Supporting Fig. S19). This indicates that they may have also

597 grown from rift-stored melts with higher Nb/Y ratios, and these crystals were recycled into the lower  
598 Nb/Y Phase 3 melts.

599 Overall, melt inclusion Nb/Y ratios indicate that melt inclusions erupted in the first 2 weeks of 2018  
600 likely crystallized from a single parent magma body (or a series of magma bodies with similar  
601 parental magmas), and that very few melt inclusions crystallized following mixing between rift-  
602 stored and Phase 3 melts (although crystal recycling between different stored magma batches did  
603 occur).

#### 604 4.5 Pre-eruptive magma storage depths

605 Melt inclusion H<sub>2</sub>O and CO<sub>2</sub> contents provide further constraints on the nature of magma storage  
606 within the LERZ. The increase in H<sub>2</sub>O and decrease in CO<sub>2</sub> with decreasing MgO content (Fig. 3c-d)  
607 provide strong evidence that melts were volatile-saturated throughout the fractionation interval  
608 considered here. Thus, estimates of the melt inclusion temperature, major elements, H<sub>2</sub>O and CO<sub>2</sub>  
609 contents at the time of entrapment may be used to calculate the pressure at which those dissolved  
610 volatile contents would be saturated, and, by extension, the pressure at which the melt inclusion  
611 was trapped within its host crystal. This is termed the “saturation pressure”, or “entrapment  
612 pressure”. By estimating the crustal density profile, these saturation pressures can be converted into  
613 depths within the volcanic edifice.

614 As discussed in section 4.2, H<sub>2</sub>O-CO<sub>2</sub> systematics indicate that a number of melt inclusions were  
615 likely trapped during ascent, after degassing had begun. While these still yield useful saturation  
616 pressures (indicating the depths at which inclusions are forming on the way to the surface), we also  
617 filter the dataset to only consider melt inclusions trapped from magmas prior to the onset of  
618 degassing on ascent to identify magma storage reservoirs. To remove melt inclusions trapped during  
619 degassing, we exclude inclusions with CO<sub>2</sub> contents lying more than 30% below the CO<sub>2</sub> content  
620 predicted by MELTS model B at the MgO content of each melt inclusion. To remove inclusions which  
621 have undergone H<sub>2</sub>O degassing or diffusive re-equilibration, we filter inclusions more than ±30%  
622 from MELTS model B. An example of this filtering process is shown in Fig. 6d-f for F17 melt  
623 inclusions. Melt inclusions meeting both criteria are marked with red crosses (see also Supporting  
624 Fig. S20).

625 We use the solubility model MagmaSat (Ghiorso and Gualda, 2015) implemented in the Python3 tool  
626 VESlcal (v.0.01; Iacovino et al., 2021) to calculate entrapment pressures from PEC-corrected major  
627 element, H<sub>2</sub>O, and CO<sub>2</sub> contents of each melt inclusion, and a temperature estimated using the Helz  
628 and Thornber (1987) MgO thermometer. We choose MagmaSat because this model provides the  
629 best fit of available models to experimental data with basaltic to dacitic compositions, as a result of  
630 its thermodynamic nature and extensive calibration dataset (Wieser et al., in press). Additionally,  
631 use of this model provides consistency with our models of volatile solubility during fractionation and  
632 ascent, as MagmaSat is the solubility model used in Rhyolite-MELTS v.1.2.0.

633 Filtered early phase 1 melt inclusions show a distinct clustering of saturation pressures at ~0.48-0.8  
634 kbar, with 4 inclusions spanning pressures up to 1.15 kbars (Fig. 8a). Filtered F17 melt inclusions  
635 show a remarkable overlap with Early Phase 1, mostly spanning 0.55 – 0.8 kbar, with 2 higher  
636 pressure inclusions (Fig. 8b). Only two melt inclusions from F13-react and five from F20 pass our  
637 filters (Fig. 6a, c, Fig. 8c-d, Supporting Fig. S20), but these also yield very similar pressure distributions.  
638 Unfiltered data for all samples stretches to significantly lower pressures, indicating that a number of

639 melt inclusions were likely trapped during ascent (fig. 8e-h). It is worth noting that melt inclusions  
640 from F13-react and F20 samples show clusters at 0.01-0.03 wt% CO<sub>2</sub>, which could indicate that a  
641 large number of inclusions were trapped during degassing, or that these fissures were tapping a  
642 slightly shallower magma reservoir.

643 Using a crustal density of  $\rho = 2,600 \text{ kg/m}^3$  based on the relationship between drill depth and pressure  
644 presented from borehole drilling results at Puna Geothermal Venture from Teplow et al. (2009), melt  
645 inclusion saturation pressures can be converted into magma storage depths. Filtered melt inclusions  
646 cluster between ~2 and 3 km (Figure 8), which aligns remarkably well with the depth at which an  
647 even more silicic dacitic magma was drilled at the PGV injection well KS-13 in 2005 (depth of 2,488 m,  
648 ~650 bars pressure, yellow star on Figure 8). There is also an interesting correspondence between  
649 our saturation depths and the depth of a low  $V_b/V_s$  anomaly imaged in this area between  
650 Pu'uhonua'ula and Pu'ulena Crater (Figure 1b, ~2km depth, vertical extent of 1.5 km, P. Cooper &  
651 Dustman, 1995). This anomaly has been interpreted as a geothermal reservoir with steam-filled  
652 cracks. The lateral dimensions of this body (2.5 km parallel to the rift zone, 2 km perpendicular to the  
653 rift zone) means that it directly underlies the fissures erupted in the first 2 weeks of the 2018  
654 eruption. It seems highly probable that the magma body being tapped by the 2018 eruption lies  
655 directly beneath this geothermal reservoir, providing a heat source.

#### 656 4.6 Temporal evolution of Kīlauea's LERZ

657 We present a schematic model summarizing the evolution of Kīlauea's LERZ, based on our findings  
658 and previous work on historic lava samples (Fig. 9). The early fissures of the 1955 eruption, which  
659 are located very close to the 2018 eruption site (Fig. 1c), tapped melts with whole-rock contents of ~  
660 5-5.7 wt% MgO. These melts were likely resident in the rift zone since at least since 1924 (when a  
661 dike swarm propagated past the 2018 eruption site into Kapoho) or 1790 (the last eruption where  
662 magma breached the surface in this section of the LERZ; Fig. 1c). Alternatively, <sup>230</sup>Th-<sup>226</sup>Ra dating of  
663 1955E lavas suggests that clinopyroxenes and plagioclases were resident for at least 550 years prior  
664 to eruption. The later phases of the 1955 eruption focused at fissures uprift of the 2018 eruption site  
665 tapped more MgO-rich magmas (6.2-6.8 wt% MgO<sub>Whole-rock</sub>) which have been interpreted to reflect  
666 renewed supply from the summit reservoir (Helz and Wright, 1992; Fig. 9a). This resupply may have  
667 propagated downrift, helping to replenish reservoirs depleted during the early phases of the 1955  
668 eruption. In 1960, activity commenced downrift of the 1955E fissures, first trapping stored magma  
669 with chemical similarities to the 1955 lavas (6.1-6.6 wt% MgO<sub>Whole-rock</sub>), followed by the appearance  
670 of progressively higher MgO contents associated with supply of material from Kīlauea's summit  
671 reservoir (7-13 wt% MgO<sub>Whole-rock</sub>, Russell and Stanley, 1990). As in the later phases of the 1955  
672 eruption, the 1960 summit resupply may also have replenished the larger reservoir complex residing  
673 beneath the 2018 eruption site (as the 1960 magmas are very similar in terms of Nb/Y and major  
674 elements; Russell and Stanley, 1990, Fig. 9b). This pulse of activity in 1955-1960 left substantial  
675 amounts of magma at depth, which continued to cool and fractionate over the next 60 years as  
676 activity shifted to Kīlauea's summit, South West Rift Zone and Middle East Rift Zone. In 2005, a  
677 dacitic pocket of magma was encountered during geothermal drilling (Fig. 9c).

678 The propagation of a dike downrift from Pu'ū'ō'ō on April 30<sup>th</sup>, 2018, disturbed these rift-stored  
679 melts, with magma erupting at the surface beginning on May 3<sup>rd</sup> (Fig. 9d). After a short pause after  
680 May 9<sup>th</sup>, erupted melt compositions between the 12-18<sup>th</sup> of May begin to show mixing between  
681 LERZ-stored and dike-supplied melts (e.g. in matrix glass Nb/Y ratios, Fig. 4a, Gansecki et al., 2019,  
682 Supporting Fig. S18), although erupted crystals are still dominated by geochemical signatures

683 indicative of the LERZ-stored component (Fig. 4c-d). Dacitic melts also began erupting at F17, and  
684 Fissure 13 shows mixing between these dacitic melts and the more MgO-rich LERZ-stored  
685 component. By the time activity focused at Ahu'ailā'au (F8) on May 28<sup>th</sup>, almost all LERZ-stored  
686 crystals (and melts) had been flushed out by dike stored material (Fig. 9e, Fig. 4d, Supporting Fig.  
687 S19).

688 It is noteworthy that Early Phase 1 lavas have similar MgO contents of early 1955 lavas, so if these  
689 are the parent, the portion of the reservoir tapped by Early Phase 1 fissures must have been  
690 sufficiently thermally buffered that minimal fractionation took place over ~60 years. Relatively slow  
691 cooling rates within a thermally buffered magma body are consistent with ~500 year residence times  
692 inferred for the early 1955 lavas by Cooper et al. (2001). Alternatively, the 1955E reservoir may have  
693 been topped up by more MgO-rich magma in the later phases of the 1955 eruption or the 1960  
694 eruption (Fig. 9b).

695 The larger amount of fractional crystallization experienced by F17 melts erupting on May 14<sup>th</sup> and  
696 the dacitic magma encountered during drilling in 2005 compared to melts erupted between May 3-  
697 9<sup>th</sup> is intriguing. The similarity of melt inclusion saturation pressures and drilling depths between all  
698 three samples, and similarity of Nb/Y ratios between Early Phase 1 and F17 from these samples  
699 indicate that the melts supplying all three bodies had a similar parent magma, and were stored at a  
700 similar depth. We suggest that the F17 dacitic melt may have formed on the periphery of the larger  
701 magma body located in this region, allowing more cooling to occur in a specific amount of time (Fig.  
702 9d). This interpretation is supported by the fact that F17 is offset ~220 m NE from the trend defined  
703 by other fissures. Pockets of dacitic melt may also have formed within regions of enhanced  
704 hydrothermal cooling. Deconvolving the nature of the evolution of this complex LERZ magma body  
705 in space and time will likely require detailed thermal modelling, and isotopic data to provide a more  
706 precise way to identify different magma batches with more resolution than can be achieved using  
707 incompatible trace element ratios.

## 708 5. Global occurrence of more silicic melts in basalt-dominated 709 volcanic region

710 Analyses of erupted matrix glasses and melt inclusions from the 2018 eruption demonstrate that  
711 extensive crystallization of an ocean island basalt causes substantial enrichment in incompatible  
712 volatile and trace element species (Cl, F, H<sub>2</sub>O). In particular, the increase in melt H<sub>2</sub>O contents  
713 combined with a rapid increase in melt viscosity following Fe-Ti oxide fractionation means that these  
714 silicic magmas have the potential to display more explosive eruption styles relative to the more  
715 typical Hawaiian style exhibited by basaltic to basaltic-andesite magmas.

716 The eruption of dacitic melt in 2018 at Kīlauea provides support to the growing volume of literature  
717 indicating that andesitic-rhyolitic magmas are more common than we thought in predominantly  
718 basalt-dominated volcanic regions. For example, Stock et al. (2020) report low An plagioclase crystals  
719 (down to An<sub>48</sub>) in basaltic lava and reticulite dominated by a higher An plagioclase population (An<sub>78-  
720 82</sub>) from the 2015 eruption of Volcan Wolf in the Galapagos Archipelego. They also identify low An  
721 plagioclase crystals in gabbroic nodules from the 1968 Fernandina eruption. Fractionation models  
722 indicate that these plagioclase crystals must have grown from basaltic trachy-andesite and trachy-  
723 andesitic melts. Additionally, resorbed quartz has been identified in tephra from the 2015 eruption  
724 of Wolf. This indicates that the subvolcanic plumbing system at these two volcanoes which erupt

725 monotonous basaltic compositions must contain highly fractionated, silicic melts at depth not yet  
726 observed at the surface.

727 Rhyolites comprise approximately 10% of erupted lavas in Iceland (Jónasson, 2007), and have been  
728 noted in a variety of settings among mid-oceanic ridges (Wanless et al., 2010). While the continuum  
729 of melt inclusion major element contents from basalt to dacite, and good fit of major, volatile and  
730 trace element contents to MELTS fractional crystallization models indicate that Kīlauea dacites result  
731 from extensive fractional crystallization, silicic magma occurrences in Iceland and MOR have been  
732 variably attributed to fractional crystallization, crystal-melt segregation, and partial melting of  
733 hydrothermally altered crust based on isotopic, volatile, major and trace element data (Elders et al.,  
734 2011; Geist et al., 2021; Masotta et al., 2018; Rooyackers et al., 2021a; Wanless et al., 2010).

735 Interestingly, Rooyackers et al. (2021b) highlight the fact that silicic magmas have been encountered  
736 4 times in the last two decades years during borehole drilling: dacite at Kīlauea (Teplow et al., 2009),  
737 trachyte in Menegai, Kenya (Mbia et al., 2015), and rhyolite on two occasions at Krafla (Elders et al.,  
738 2011; Mortensen et al., 2010). While the Menegai and Krafla drilling encounters were a little less  
739 surprising in terms of the composition encountered compared to Kīlauea (because rhyolitic and  
740 syenetic magmas are better represented in surface deposits at these locations), It is noteworthy that  
741 all of these encounters intercepted silicic magmas at very similar depths (2488 m at Kīlauea, ~2000  
742 m in Kenya, 2571 m and 2104 m at Krafla), all in areas of active hydrothermal exploration. Although  
743 these silicic magmas may be generated by different mechanisms, all require high heat fluxes at  
744 shallow levels, either to melt/rejuvenate existing material, or to allow fractional crystallization to  
745 proceed without the magma simply freezing in the crust. At Kīlauea, this high heat flow likely results  
746 from the focus of repeated intrusion over hundreds of years in this particular section of the rift zone,  
747 perhaps resulting from a “jog” in the rift zone, with two offset branches creating a local extension  
748 stress field (Kenedi et al., 2010). This is somewhat analogous to the higher focusing of melt, and  
749 therefore higher occurrence of silicic magma in overlapping spreading centers of mid-oceanic ridges  
750 (Kent et al., 2000).

751 While 2018 marked the first documented occurrence of dacitic melt erupting at the surface, given  
752 that 70% of Kīlauea’s surface is <500 yrs old, and 90% is <1100 yrs old (Holcomb, 1987), these melts  
753 could erupt on a centurial-millennial basis, and still be absent in surface exposures. This is particularly  
754 true given that dacitic melts are most likely to form in parts of the volcano characterised by high  
755 intrusion rates, to maintain the high heat fluxes at shallow levels required for melts to fractionate to  
756 dacitic compositions without freezing in the crust. In turn, high intrusion rates mean these sites are  
757 most likely to be rapidly resurfaced by volcanic activity. For example, 75% of the surface of the  
758 lower-east rift zone is <500 yrs old (Moore, 1992) . If magmas with silicic compositions were able to  
759 evade sampling at Kīlauea, one of the world’s best-studied ocean island volcanoes, prior to drilling in  
760 2005, it seems highly likely that these compositions are present at other ocean island volcanoes.  
761 Specifically, based on the need for high heat flow to generate silicic magma bodies, and the  
762 increasing number of drilling encounters, the anomalously hot areas of ocean islands are not only  
763 the most likely to contain more silicic melts at shallow depths, but will also be the preferred targets  
764 for hydrothermal exploration.

765 When the dacitic body was drilled at Kīlauea in 2005 at 2488 m depth, it was noted that the glass  
766 did not show vesiculation (Teplow et al 2009), leading to inferences that the magma was volatile-  
767 poor. Given that our melt inclusion measurements demonstrate that F17 melts were H<sub>2</sub>O-rich, we



768 instead hypothesize that the low vesicularity resulted from the fact that a relatively small mass of  
769 volatiles is exsolved during fractionation from a basalt to dacite (~0.04 wt%) at this depth, meaning  
770 there is limited potential for a large, gas-rich cap to develop on top of these bodies (Fig. 5a). Upon  
771 ascent, significant quantities of H<sub>2</sub>O only begin to exsolve from a dacitic melt composition at ~300  
772 bars. Thus, as long as the drilling fluid quenches these silicic melts at higher confining pressures,  
773 there would be limited potential for large amounts of volatile exsolution and catastrophic well  
774 blowout (Teplow et al., 2009). However, if allowed to rise to shallow levels prior to quenching, silicic  
775 melts could present a hazard to geothermal drilling in basalt-dominated settings.

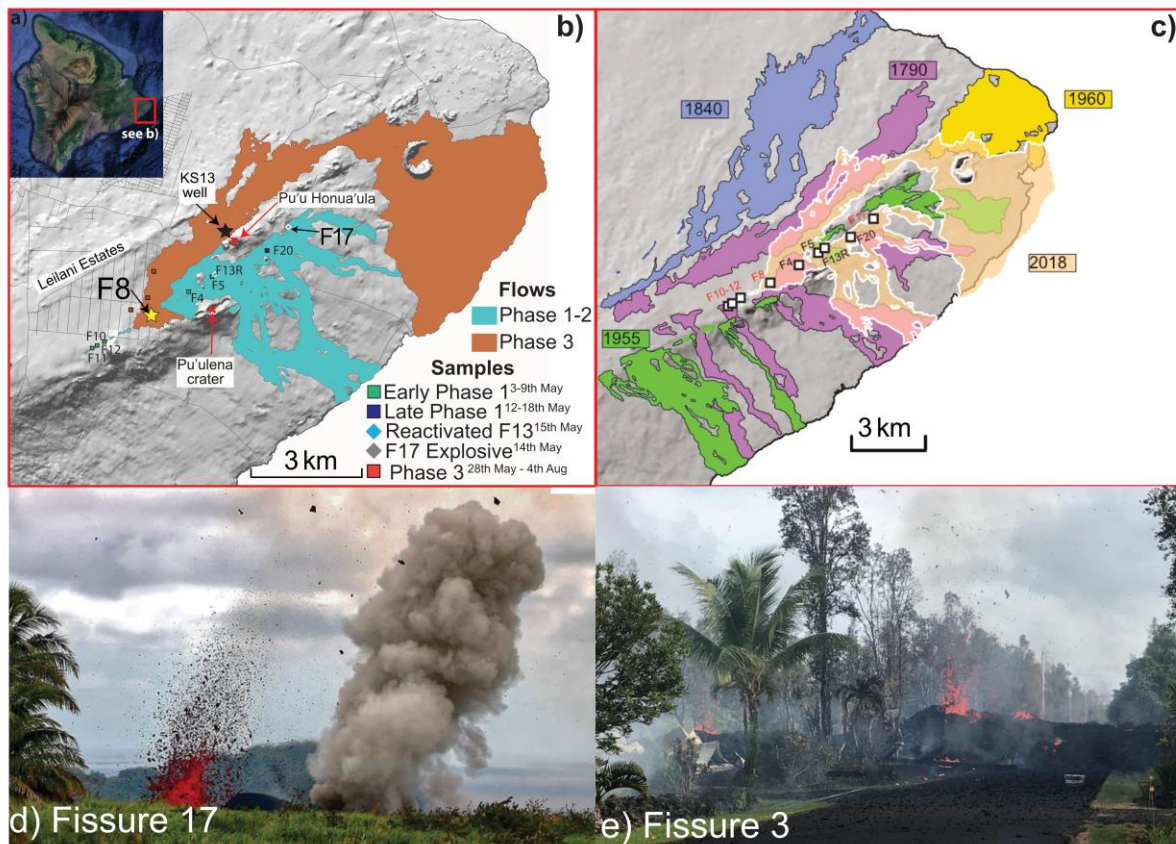
776 In addition to being encountered during drilling, it appears that the eruption of silicic melts at the  
777 surface may be closely coupled to the injection of basaltic dikes into the region. At Kīlauea, based on  
778 the limited evidence for mixing between the dacite and the dike-supplied magma in the initial  
779 products of F17, we suggest that dike injection increased overpressure or changed the stress state in  
780 the magma body, causing the eruption. Similarly, Rooyakkers et al., (2021b) examine the rhyolitic  
781 magma producing the Víti maar at Krafla, Iceland, and conclude that these melts show very little  
782 textural or chemical evidence for mingling/mixing with the basaltic “trigger”. This contrasts with  
783 explosive eruptions like Askja, 1875 which show clear evidence textural evidence for pre-eruptive  
784 magma mixing (Sparks et al., 1977). Clearly, the potential of silicic magma bodies to generate  
785 explosive eruptions should be considered during hazard assessments in a wide variety of ocean  
786 islands and other basalt-dominated settings (Rooyakkers et al., 2021b), both in terms of natural  
787 eruptions initiated by a dike, and drilling encounters.

## 788 6. Conclusions

789 Basaltic to andesitic magmas erupted during the first two weeks of the 2018 eruption (3<sup>rd</sup> – 16<sup>th</sup>  
790 May) were likely formed from variable amounts of crystallization of a magma body at ~2-3 km depth  
791 within the LERZ. The similarity in Nb/Y ratios in melt inclusions from these early eruptive fissures and  
792 a range of host crystal chemistry implies that crystallization proceeded from a single magma parent  
793 body (or a series of bodies with near-identical trace element chemistry). Comparison of Nb/Y ratios  
794 to historic LERZ lavas indicates that melts erupted in 1955-1960 are the most likely parent to the  
795 early 2018 lavas (see also Helz, 2008; Pietruszka et al., 2021; Teplow et al., 2009). Extensive  
796 crystallization of a section of this larger magma body (perhaps on the periphery or in a region with  
797 enhanced hydrothermal cooling) produced a dacitic melt composition highly enriched in  
798 incompatible elements such as Cl, F, Zr, and H<sub>2</sub>O. Combined with an increase in magma viscosity with  
799 increasing SiO<sub>2</sub> content and dropping temperatures, this H<sub>2</sub>O-enrichment accounts for the explosive  
800 strombolian behavior exhibited by the eruptive fissure tapping this melt (F17) without requiring  
801 external sources of volatiles such as groundwater. Although the high viscosities of these dacitic melts  
802 mean they are unlikely to erupt spontaneously, the 2018 eruption shows that they may be triggered  
803 by the injection of basaltic intrusion. The volatile-rich nature of these bodies should also be  
804 considered when prospecting for geothermal wells; if the melt erupted at F17 had been drilled and  
805 allowed to depressurize to ~300 bars prior to quenching, large amounts of vesiculation may occur.

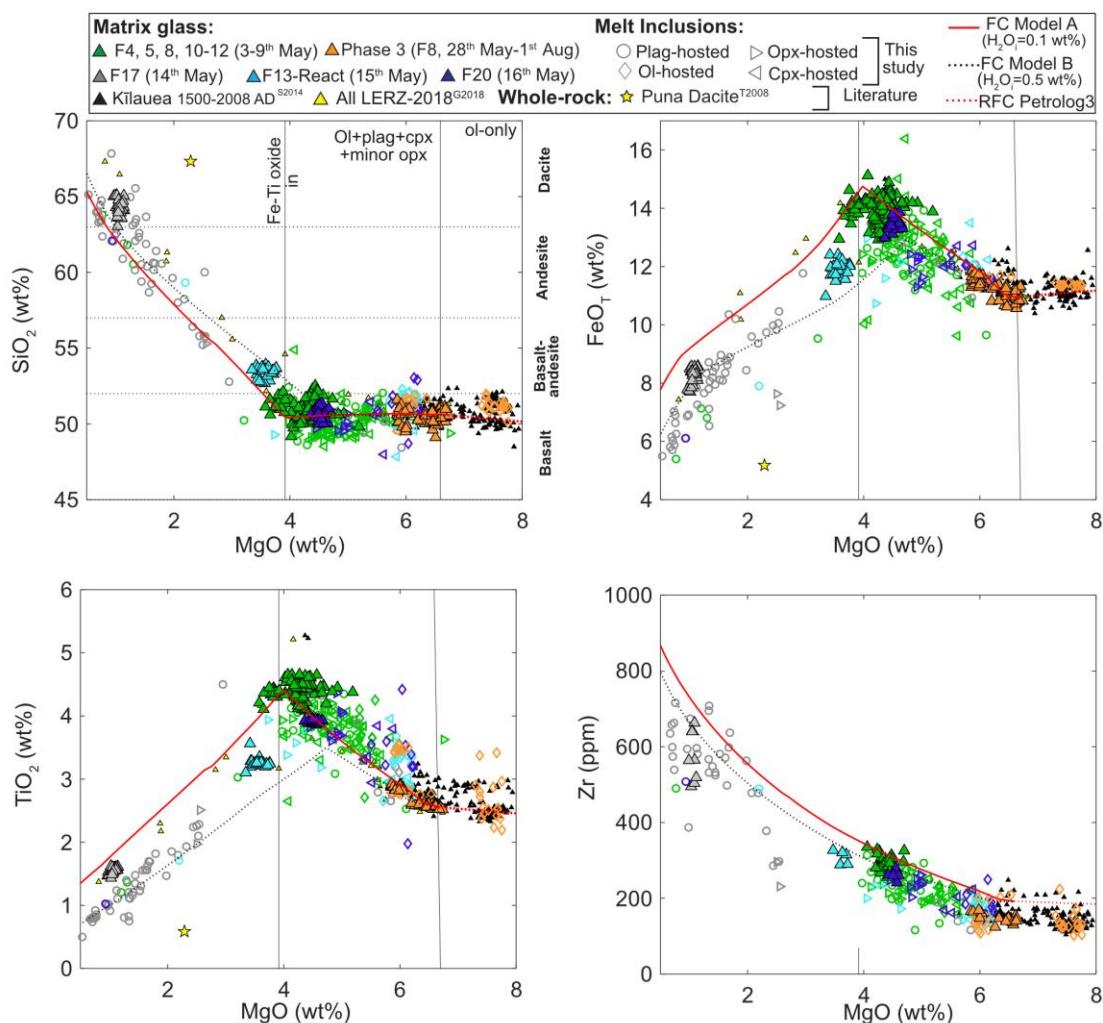
## 806 Figures

807 (see attached pdfs for higher resolution figs)



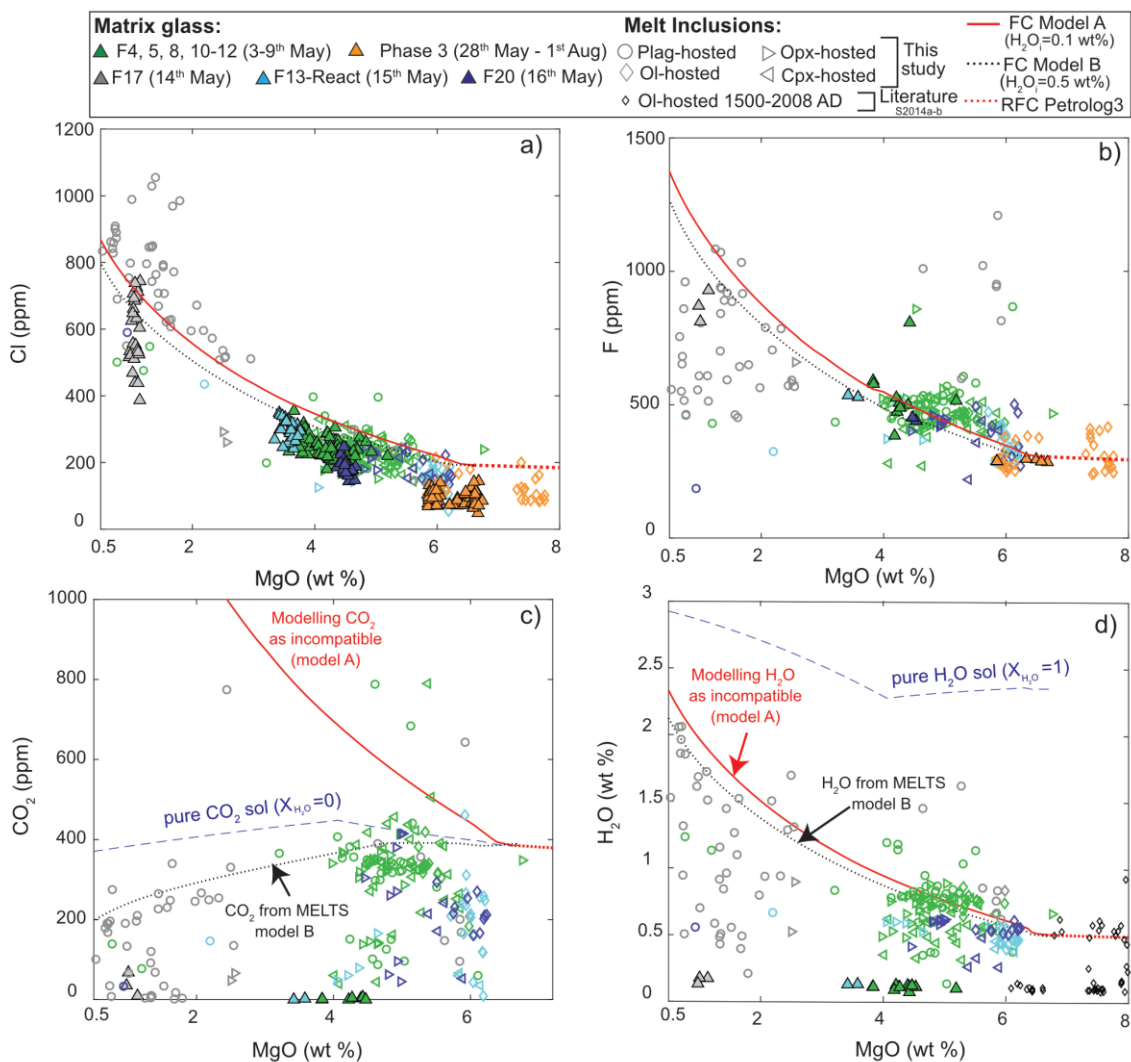
808

809 Figure 1 – a) Map of the island of Hawai'i, with the area inside the red box expanded in b). b)  
 810 Hillshade map from DEM of the Lower East Rift Zone showing the fissures and lava flows produced  
 811 during the 2018 eruption. Locations of samples analysed in this study are shown with colored  
 812 symbols. Ahu'ailā'au (F8) is marked with a yellow star, and the location of borehole KS13 where a  
 813 dacitic magma was drilled in 2005 is shown with a black star. Pu'u honua'ula and Pu'ulena Crater are  
 814 marked with red crosses (reference points for the position of the seismic anomaly). c) Map showing  
 815 the location of previous eruptive episodes on the LERZ, with the 2018 flows overlain in pale pink. d)  
 816 F17 showing the difference in eruption style between the basaltic-andesite eastern end (low  
 817 fountaining and spattering, LHS), and the more silicic andesitic western end (strombolian explosions  
 818 and gas jetting, RHS). e) Low spatter mounds produced during the first day of the eruption at F3.  
 819 Photos in d and e) from USGS. Part b) was adapted from Patrick et al., (2019), and c) from Pietruszka  
 820 et al., (2021), using geospatial data from Trusdell et al., 2006; Zoeller et al., 2020



821

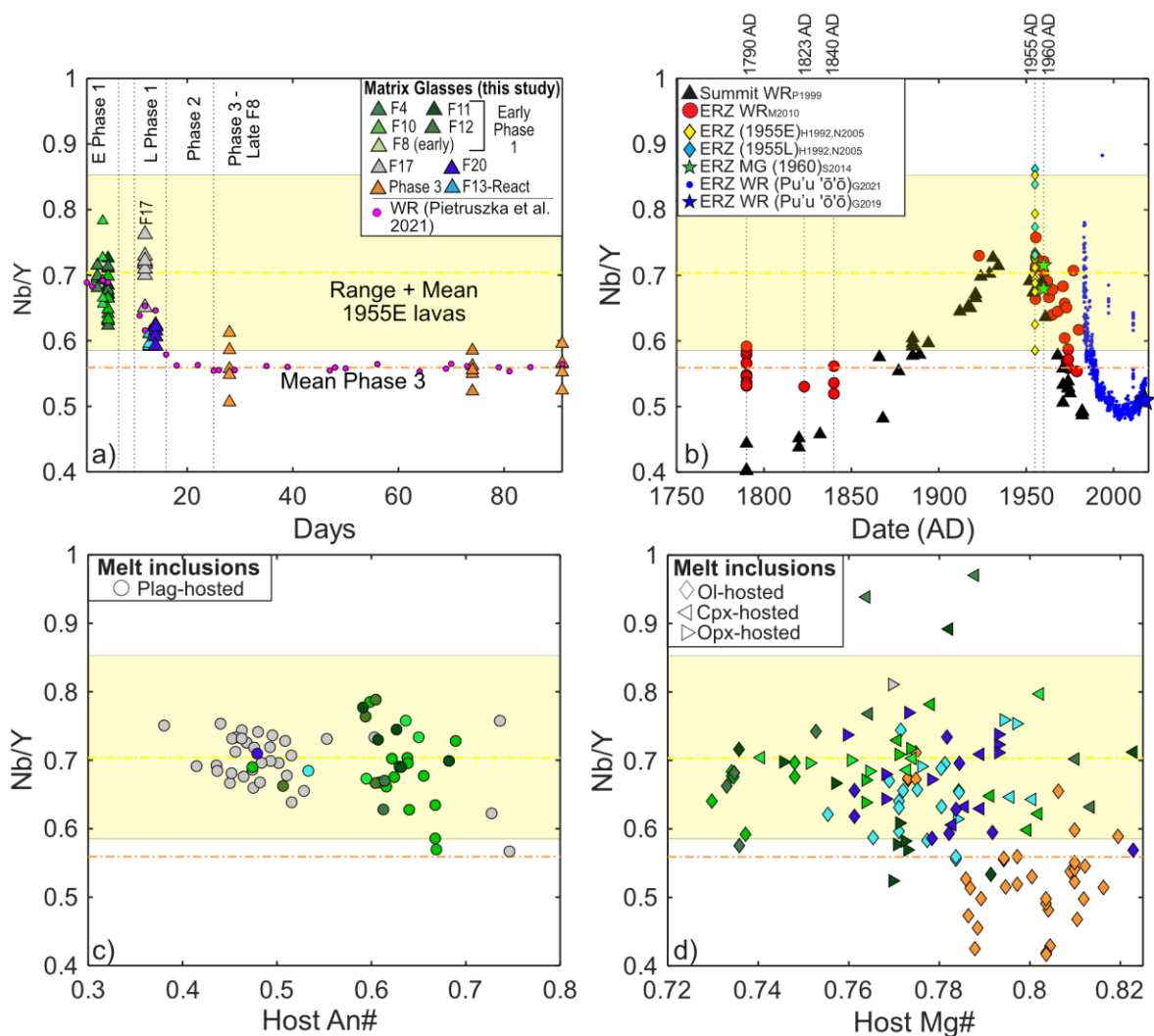
822 Figure 2- Major element systematics of matrix glasses and melt inclusions. The composition of  
 823 olivine, clinopyroxene and 6 plagioclase melt inclusions are corrected for the effects of PEC.  
 824 Literature data for matrix glasses erupted during the 2018 eruption (yellow triangles, Gansecki et al.,  
 825 2019) and previous Kilauea eruptions (black triangles, Sides et al., 2014a, 2014b; Wieser et al., 2019)  
 826 are shown, along with the whole-rock composition of the dacitic magma drilled in 2005 (Teplow et  
 827 al., 2009). Two fractional crystallization models run in alphaMELTS for MATLAB (Rhyolite-MELTS  
 828 v1.2.0, Antoshechkina and Ghiorso, 2018; Ghiorso and Gualda, 2015; Gualda et al., 2012) are shown,  
 829 with  $Fe^{3+}/Fe_T$ , initial=0.15 (unbuffered),  $P=650$  bars. Model A uses an initial  $H_2O$  content of 0.1 wt%  
 830 (red line, best recreates the onset of Fe-Ti oxide saturation), while Model B uses a more realistic  
 831 initial  $H_2O$  content of 0.5 wt% (black dashed line). As the rhyolite-MELTS model fails to recreate the  
 832 olivine-only fractionation assemblage at  $>6.8$  wt% (Wright and Fiske, 1971), the red dashed line  
 833 shows a reverse fractionation crystallization (RFC) model run from the starting composition in  
 834 Petrolog3.1.3 (Danyushevsky and Plechov, 2011). The fractionation trajectory for Zr is calculated  
 835 assuming incompatible behavior.



836

837 Figure 3– Volatile element systematics, with fractionation trajectories assuming perfect  
 838 incompatibility for all elements from MELTS model A shown in red. Incompatible behavior is  
 839 assumed for Cl and F in MELTS model B, while CO<sub>2</sub> and H<sub>2</sub>O solubility in equilibrium with a mixed  
 840 fluid are tracked in the solubility model MagmaSat integrated into MELTS (dashed black line). The  
 841 dashed red section of the line shows reverse crystallization of olivine from the starting composition  
 842 in Petrolog3. For Cl and F, models A and B produce very similar trajectories, as these models predict  
 843 similar amounts of solid fractionated. The solubility of pure CO<sub>2</sub> and H<sub>2</sub>O calculated using the  
 844 MagmaSat solubility model (Ghiorso and Gualda, 2015) implemented in VESlcal (Iacovino et al.,  
 845 2021) for a best-fit to the observed major element path (see Supporting Fig. S11) is shown with a  
 846 blue dashed line.





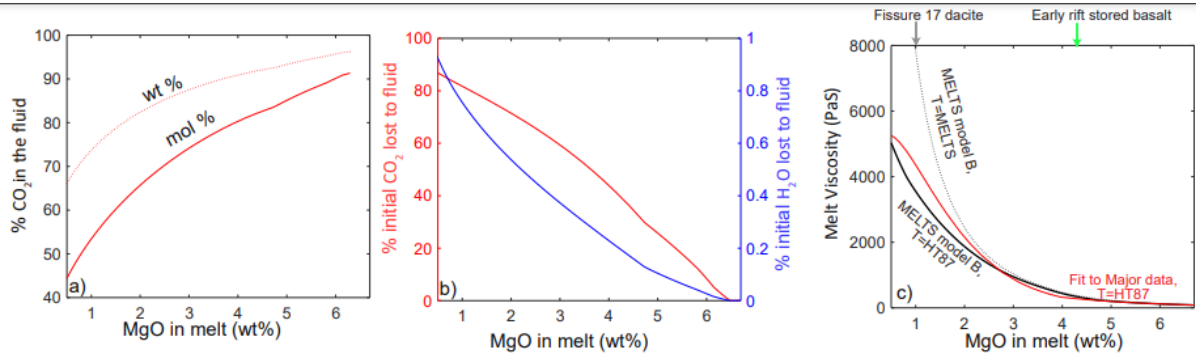
847

848

849 Figure 4– Ratios of incompatible trace elements in 2018 eruption products and previous LERZ  
 850 eruptions. **a)** variations in Nb/Y in co-erupted matrix glasses (this study) with time throughout the  
 851 eruption (May 3<sup>rd</sup> = Day 1). Whole-rock measurements from Pietruszka et al. (2021) are overlain. **b)**  
 852 Compilation of Nb/Y ratios versus time for whole-rock measurements of summit lavas (black  
 853 triangles, Pietruszka and Garcia, 1999), LERZ lavas from 1790, 1823, 1840, 1955, 1960 (red dots,  
 854 Marske, 2010), early phases of the 1955 LERZ eruption (yellow colors), and later phases (cyan colors,  
 855 Helz and Wright, 1992; Norman, 2005). Analyses of matrix glass from the 1960 Kapoho eruption  
 856 from Sides et al., (2014b) and whole-rock measurements from Pu'u'ō'ō are also shown (Gansecki et  
 857 al., 2019; Garcia et al., 2021). The mean composition of the early 1955 lavas and Phase 3 matrix  
 858 glasses are shown with a yellow and orange dashed line on all plots, with the range for 1955 shown  
 859 in light yellow. **c)** Nb/Y ratios in plagioclase-hosted melt inclusions vs. host anorthite content. **d)**  
 860 Nb/Y ratios vs. host Mg# for olivine, orthopyroxene and clinopyroxene-hosted melt inclusions.  
 861 Symbols in part c-d are colored by fissure as in part b.



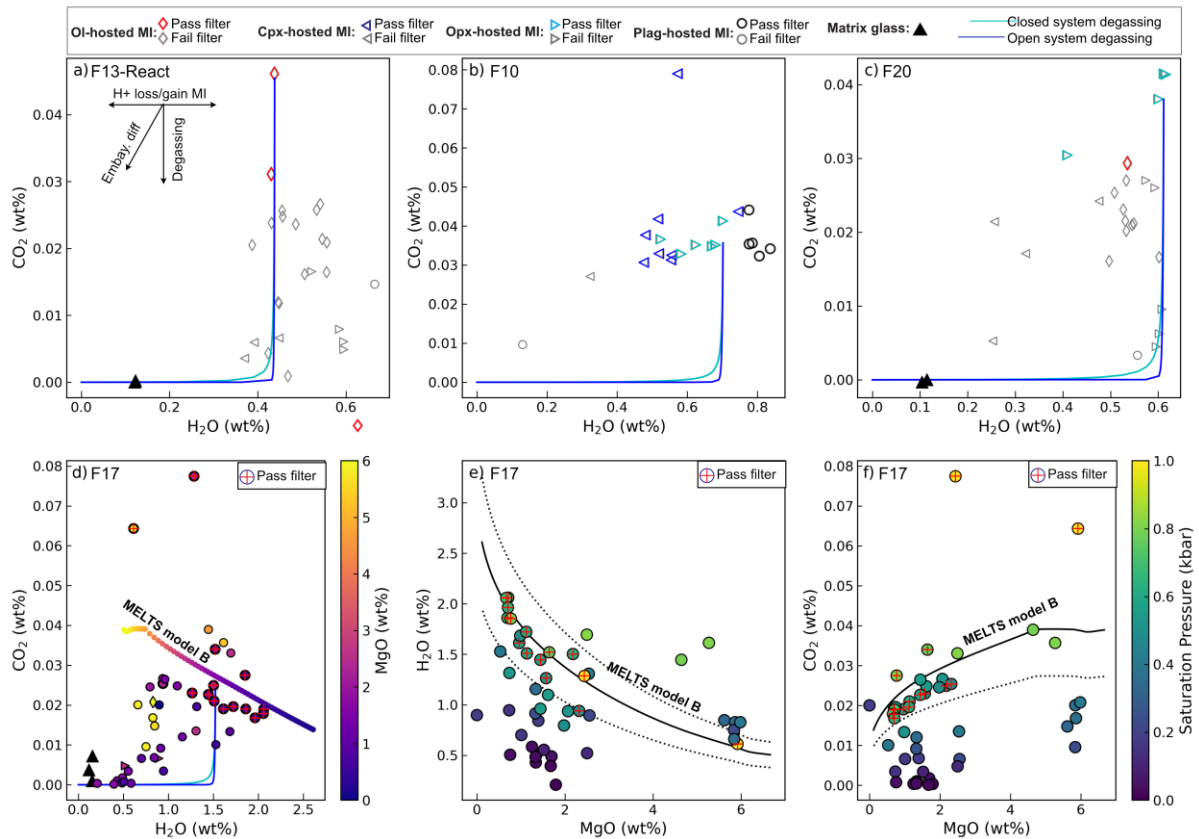
862



863

864

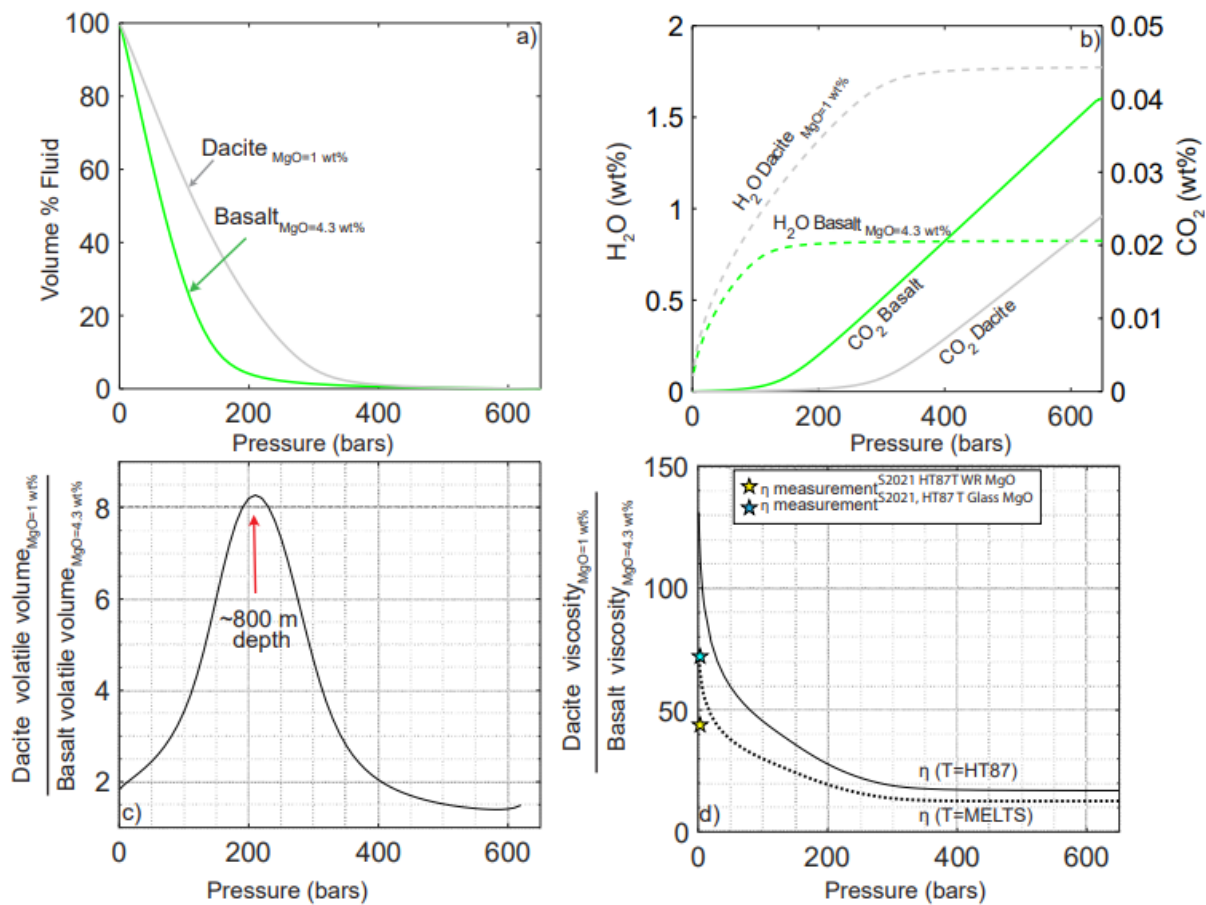
865 Figure 5- Volatile exsolution and changes in viscosity during fractional crystallization tracked in  
 866 MELTS model B. **a)** % of CO<sub>2</sub> in the exsolved fluid (by wt% and mol%) decreases with progressive  
 867 fractionation. **b)** % of the initial amount of CO<sub>2</sub> (red solid line) and H<sub>2</sub>O (blue solid line) lost to the  
 868 fluid phase during fractionation. **c)** Changes in viscosity during fractionation. The black dashed line  
 869 shows viscosity from MELTS model B using Giordano et al., (2008) and the MELTS temperature, and  
 870 the black solid line shows MELTS model B with temperatures calculated from the MELTS MgO  
 871 content using the Helz and Thornber (1987) MgO thermometer. The red line shows the viscosity  
 872 calculated using Giordano et al., (2008) for the best-fit model to measured major elements  
 873 (Supporting Fig. S11), with temperatures calculated using Helz and Thornber (1987), and H<sub>2</sub>O  
 874 contents estimated for a parameterization of the relationship between H<sub>2</sub>O and MgO shown as a red  
 875 line in Fig. 3d.



876

877 Fig. 6. a-c) Example degassing paths for three fissures, with open and closed system degassing paths  
 878 calculated using MagmaSat (Ghiorso and Gualda, 2015) in VESlcal (Iacovino et al., 2021) for specific  
 879 melt inclusions overlain. Vectors for different processes are shown in a). d) Degassing path for F17  
 880 with melt inclusions colored by their MgO content. The trajectories caused by degassing (blue and  
 881 cyan lines) and fractional crystallization (yellow-purple line) are overlain. e-f) Example of the filtering  
 882 process used to calculate saturation pressures for F17. Only melt inclusions with CO<sub>2</sub> contents less  
 883 than 30% below the MELTS fractionation line (filtering out degassing), and only H<sub>2</sub>O contents within  
 884 +/-30% are used (filtering out degassing and H<sup>+</sup> re-equilibration to higher and lower values). Symbols  
 885 are colored by their saturation pressure, and are marked with a red cross if they pass both filters.

886

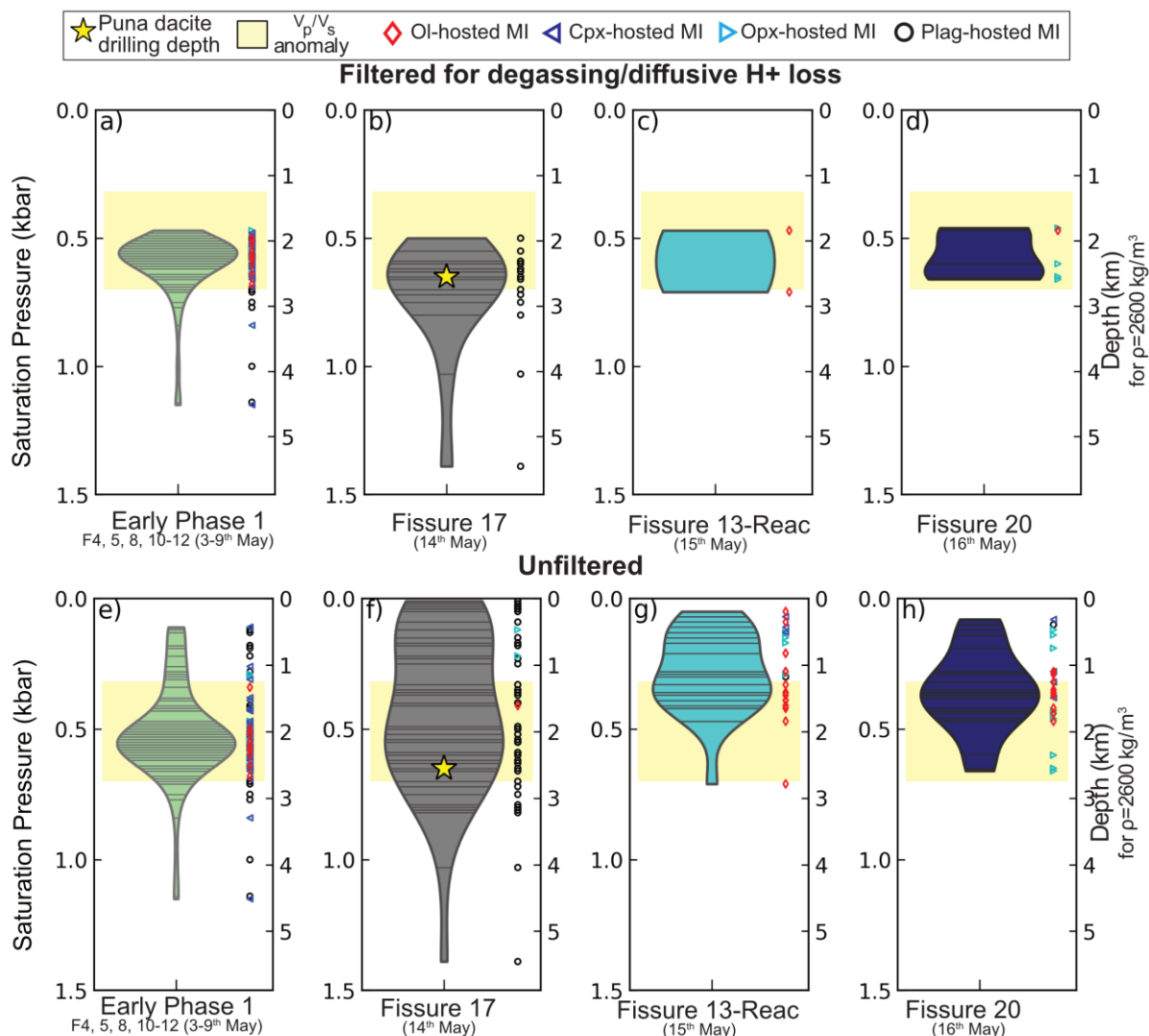


887

888 Figure 7. Volatile exsolution and changes in viscosity during ascent to the surface along a closed  
 889 system degassing path for a basaltic andesite (BA) melt (~4.3 wt% MgO, average composition of  
 890 Early Phase 1 matrix glasses), and a dacitic melt composition (MgO=1 wt%, average composition of  
 891 F17 matrix glasses). **a)** Volume of the exsolved fluid phase relative to the total volume of the system  
 892 for both melt compositions with decreasing pressure. **b)** Concentration of H<sub>2</sub>O (LH axis, dashed  
 893 lines), and CO<sub>2</sub> in the melt (RH- solid lines) during ascent. **c-d)** Comparison of the volume of volatiles  
 894 and viscosity during ascent of the dacitic and basaltic andesite melt. **c).** The volume of exsolved  
 895 volatiles is ~8-9 times higher for the dacite at ~200 bars (800 m depth), because of the higher H<sub>2</sub>O  
 896 content of this melt, and the earlier exsolution of H<sub>2</sub>O from this melt relative to the basalt (**b**). Even  
 897 at the surface, the volume of exsolved volatiles is ~2 times higher for the dacite. **d)** The viscosity of  
 898 the dacite divided by the viscosity of the basalt at each point on the ascent path calculated using the  
 899 Giordano et al., 2008 model. The dashed line shows viscosity using the temperature from MELTS,  
 900 and the solid line shows temperature calculated from the MELTS MgO content using Helz and  
 901 Thornber (1987). The yellow star shows the viscosity ratio between the dacitic F17 lavas and the  
 902 basaltic/basaltic-andesite Early phase 1 lavas reported by Soldati and Dingwell, (2021), using  
 903 temperatures they calculate from whole-rock MgO contents using Helz and Thornber (1987). The  
 904 cyan star uses their viscosity parameters (A, B, C) to calculate viscosity at the temperatures for the  
 905 MgO contents considered here for the dacitic melt (1 wt% MgO) and basaltic melt (4.3 wt% MgO)  
 906 using Helz and Thornber (1987). The lower MgO content of our F17 glass relative to their whole-rock  
 907 measurement result in a lower temperature, so a higher viscosity.

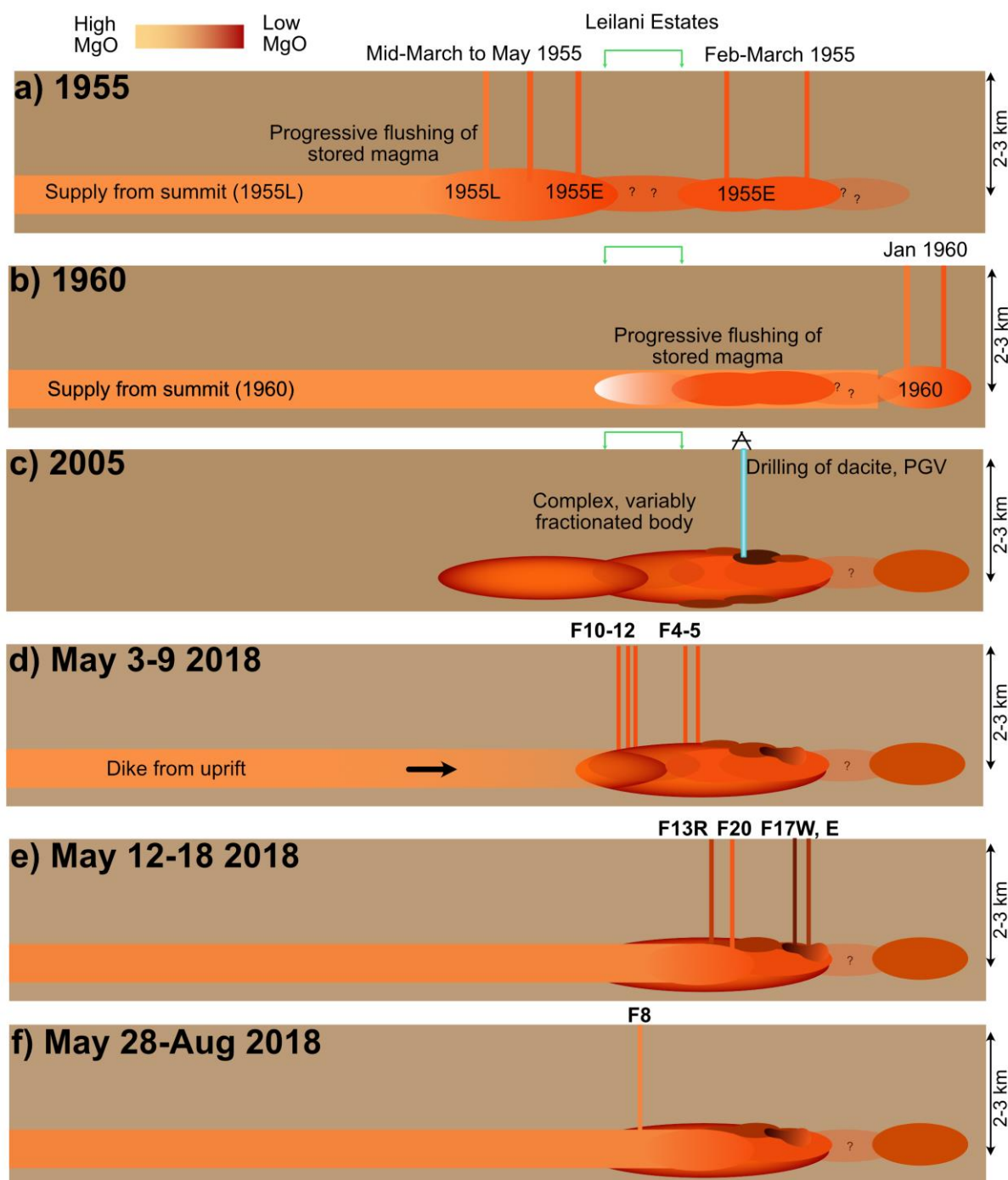
908

909



910

911 Figure 8. Magma storage depths for different early fissures from the 2018 eruption. A-h) Violin plots  
 912 showing saturation pressures calculated using the solubility model MagmaSat (Ghiorso and Gualda,  
 913 2015) implemented through VESlcal (Iacovino et al. 2021). A-d) shows filtered melt inclusions (within  
 914  $\pm 30\%$  of MELTS model B for  $H_2O$ , and  $-30\%$  for  $CO_2$ , see Fig. 6e-f). e-h) shows all melt inclusions. Each  
 915 grey line on the violin plot represents a melt inclusion, and the width of the “violin” represents the  
 916 clustering of data at each pressure. On the RHS, the individual saturation depths for each inclusion  
 917 are shown with symbol shapes and colors corresponding to the host phase. The depth at which the  
 918 dacitic magma was drilled at PGV is shown as a yellow star, and the depth of the low  $V_p/V_s$  region  
 919 (low of  $V_p/V_s=1.66$  vs.  $1.78$  background) imaged by Cooper and Dustman (1995) is shown in yellow.



920

921 Figure 9 – Schematic diagram showing evolution of the LERZ in the vicinity of the 2018 eruption site.  
 922 A) More MgO-poor stored melts (1955E) erupt between Feb-March 1955 very close to the 2018  
 923 eruption sites (Fig. 1c). More MgO-rich melts (1955L) erupt slightly uprift in mid-March to May. B)  
 924 Activity farther down the rift zone in 1960 initiates with the eruption of more MgO-poor (1955-like)  
 925 melts, followed by flushing by more MgO-rich summit magma. C) Hydrothermal drilling in 2005 taps  
 926 a dacitic body, likely located on the periphery of a complex, variably fractionated magma body. D)  
 927 Hydraulic pressure from a dike propagating downrift from Pu‘u‘ō‘ō forces stored melts to the



928 surface. E) Progressively, this dike-supplied material begins to mix with stored melts, until by May  
929 28<sup>th</sup>, this new component dominates.

## 930 Acknowledgements

931 PW acknowledges funding from a NERC DTP studentship (NE/ L002507/1), a NERC Edinburgh Ion  
932 Microprobe Facility grant (IMF675/1118), and a Cambridge University Leave to Work away grant. PA  
933 acknowledges funding for development of alphaMELTS for MATLAB by NSF through grant EAR-  
934 1947616. We also acknowledge support from the National Science Foundation ICER-20-26904,  
935 granted to OFM Research (PI. Ghiorso) for maintaining the ENKI server used to perform VESIcal  
936 calculations. PW thanks Matthew Gleeson for help running MELTS for MATLAB, including providing  
937 access to his high-powered desktop. PW thanks Iris Buisman and Guilio Lampronti for help collecting  
938 EPMA and SEM data for this study, Rod Kindel for the intrepid hike to Fissures 10, 11 and 12 in his  
939 backyard, Sarah Allen for help sampling these fissures, and Evgenia Ilyinskaya for coordinating the  
940 2018 and 2019 field campaign. We thank Emily Johnson and two anonymous reviewers, along with  
941 associate editor Ken Rubin for very helpful and detailed comments which greatly improved this  
942 manuscript.

943 Data has been archived on Zenodo (<https://zenodo.org/badge/latestdoi/417367063>) and on Github  
944 (where example MELTS for Matlab codes are also provided- [https://github.com/PennyWieser/G3-  
945 Kil2018-Evolved-MIs](https://github.com/PennyWieser/G3-Kil2018-Evolved-MIs)).

## 946 Bibliography

- 947 Antoshechkina, P., Ghiorso, M.S., 2018. MELTS for MATLAB: A new educational and research tool for  
948 computational thermodynamics. AGU.
- 949 Bauer, G.R., Fodor, R.V., Husler, J.W., Keil, K., 1973. Contributions to the mineral chemistry of  
950 Hawaiian rocks: III. Composition and mineralogy of a new rhyodacite occurrence on Oahu, Hawaii.  
951 *Contr. Mineral. and Petrol.* 40, 183–194. <https://doi.org/10.1007/BF00373783>
- 952 Cooper, K.M., Reid, M.R., Murrell, M.T., Clague, D.A., 2001. Crystal and magma residence at Kilauea  
953 Volcano, Hawaii: 230Th–226Ra dating of the 1955 east rift eruption. *Earth and Planetary Science  
954 Letters* 184, 703–718. [https://doi.org/10.1016/S0012-821X\(00\)00341-1](https://doi.org/10.1016/S0012-821X(00)00341-1)
- 955 Cooper, P., Dustman, M., 1995. Geothermal research, monitoring and testing: final report,  
956 geophysics subtask, microseismicity study. *Seismological Research Letters*.
- 957 Danyushevsky, L.V., Plechov, P., 2011. Petrolog3: Integrated software for modeling crystallization  
958 processes. *Geochemistry, Geophysics, Geosystems* 12, n/a-n/a.  
959 <https://doi.org/10.1029/2011GC003516>
- 960 Elders, W.A., Friðleifsson, G.Ó., Zierenberg, R.A., Pope, E.C., Mortensen, A.K., Guðmundsson, Á.,  
961 Lowenstern, J.B., Marks, N.E., Owens, L., Bird, D.K., Reed, M., Olsen, N.J., Schiffman, P., 2011. Origin  
962 of a rhyolite that intruded a geothermal well while drilling at the Krafla volcano, Iceland. *Geology* 39,  
963 231–234. <https://doi.org/10.1130/G31393.1>
- 964 Gaetani, G.A., O’Leary, J.A., Shimizu, N., Bucholz, C.E., Newville, M., 2012. Rapid reequilibration of  
965 H<sub>2</sub>O and oxygen fugacity in olivine-hosted melt inclusions. *Geology* 40, 915–918.  
966 <https://doi.org/10.1130/G32992.1>

- 967 Gansecki, C., Lee, R.L., Shea, T., Lundblad, S.P., Hon, K., Parcheta, C., 2019. The tangled tale of  
968 Kīlauea's 2018 eruption as told by geochemical monitoring. *Science* 366, eaaz0147.  
969 <https://doi.org/10.1126/science.aaz0147>
- 970 Garcia, M.O., Pietruszka, A.J., Norman, M.D., Rhodes, J.M., 2021. Kīlauea's Pu'u Ō'ō Eruption (1983–  
971 2018): A synthesis of magmatic processes during a prolonged basaltic event. *Chemical Geology* 581,  
972 120391. <https://doi.org/10.1016/j.chemgeo.2021.120391>
- 973 Geist, D., Harpp, K., Oswald, P., Wallace, P., Bindeman, I., Christensen, B., 2021. Hekla Revisited:  
974 Fractionation of a Magma Body at Historical Timescales. *Journal of Petrology* 62, egab001.  
975 <https://doi.org/10.1093/petrology/egab001>
- 976 Gerlach, T.M., McGee, K.A., Elias, T., Sutton, A.J., Doukas, M.P., 2002. Carbon dioxide emission rate  
977 of Kīlauea Volcano: Implications for primary magma and the summit reservoir. *Journal of*  
978 *Geophysical Research: Solid Earth* 107, ECV 3-1-ECV 3-15. <https://doi.org/10.1029/2001JB000407>
- 979 Ghiorso, M.S., Gualda, G.A.R., 2015. An H<sub>2</sub>O–CO<sub>2</sub> mixed fluid saturation model compatible with  
980 rhyolite-MELTS. *Contrib Mineral Petrol* 169, 53. <https://doi.org/10.1007/s00410-015-1141-8>
- 981 Giordano, D., Russell, J.K., Dingwell, D.B., 2008. Viscosity of magmatic liquids: A model. *Earth and*  
982 *Planetary Science Letters* 271, 123–134. <https://doi.org/10.1016/j.epsl.2008.03.038>
- 983 Gonnermann, H.M., Manga, M., 2013. Chapter 4 - Dynamics of magma ascent in the volcanic  
984 conduit, in: *Modelling Volcanic Processes. The Physics and Mathematics of Volcanism*.
- 985 Greaney, A.T., Rudnick, R.L., Helz, R.T., Gaschnig, R.M., Piccoli, P.M., Ash, R.D., 2017. The behavior of  
986 chalcophile elements during magmatic differentiation as observed in Kilauea Iki lava lake, Hawaii.  
987 *Geochimica et Cosmochimica Acta* 210, 71–96. <https://doi.org/10.1016/j.gca.2017.04.033>
- 988 Gualda, G.A.R., Ghiorso, M.S., Lemons, R.V., Carley, T.L., 2012. Rhyolite-MELTS: a Modified  
989 Calibration of MELTS Optimized for Silica-rich, Fluid-bearing Magmatic Systems. *Journal of Petrology*  
990 53, 875–890. <https://doi.org/10.1093/petrology/egr080>
- 991 Helz, R.T., 2008. How to Produce Dacitic Melt at Kilauea: Evidence from Historic Kilauea Lava.  
992 Presented at the AGU.
- 993 Helz, R.T., 1980. Crystallization history of Kilauea Iki lava lake as seen in drill core recovered in 1967–  
994 1979. *Bull Volcanol* 43, 675–701. <https://doi.org/10.1007/BF02600365>
- 995 Helz, R.T., Thornber, C.R., 1987. Geothermometry of Kilauea Iki lava lake, Hawaii. *Bulletin of*  
996 *Volcanology* 49, 651–668. <https://doi.org/10.1007/BF01080357>
- 997 Helz, R.T., Wright, T.L., 1992. Differentiation and magma mixing on Kilauea's east rift zone: A further  
998 look at the eruptions of 1955 and 1960. Part I. The late 1955 lavas. *Bulletin of Volcanology* 54, 361–  
999 384. <https://doi.org/10.1007/BF00312319>
- 1000 Holcomb, R.T., 1987. Eruptive History and Long-Term Behavior of Kilauea Volcano.
- 1001 Houghton, B.F., Gonnermann, H.M., 2008. Basaltic explosive volcanism: Constraints from deposits  
1002 and models. *Geochemistry* 68, 117–140. <https://doi.org/10.1016/j.chemer.2008.04.002>

- 1003 Houghton, B.F., Taddeucci, J., Andronico, D., Gonnermann, H.M., Pistolesi, M., Patrick, M.R., Orr,  
1004 T.R., Swanson, D.A., Edmonds, M., Gaudin, D., Carey, R.J., Scarlato, P., 2016. Stronger or longer:  
1005 Discriminating between Hawaiian and Strombolian eruption styles. *Geology* 44, 163–166.  
1006 <https://doi.org/10.1130/G37423.1>
- 1007 Iacovino, K., Matthews, S., Wieser, P.E., Moore, G., Begue, F., 2021. VESical Part I: An open-source  
1008 thermodynamic model engine for mixed volatile (H<sub>2</sub>O-CO<sub>2</sub>) solubility in silicate melt. *Earth and*  
1009 *Space Science*. <https://doi.org/10.1029/2020EA001584>
- 1010 Jaupart, C., Vergnolle, S., 1988. Laboratory models of Hawaiian and Strombolian eruptions. *Nature*  
1011 333, 58–60.
- 1012 Jenner, F.E., Hauri, E.H., Bullock, E.S., König, S., Arculus, R.J., Mavrogenes, J.A., Mikkelsen, N.,  
1013 Goddard, C., 2015. The competing effects of sulfide saturation versus degassing on the behavior of  
1014 the chalcophile elements during the differentiation of hydrous melts. *Geochemistry, Geophysics,*  
1015 *Geosystems* 16, 1490–1507. <https://doi.org/10.1002/2014GC005670>
- 1016 Johnson, E.A., Rossman, G.R., 2013. The diffusion behavior of hydrogen in plagioclase feldspar at  
1017 800-1000 C: Implications for re-equilibration of hydroxyl in volcanic phenocrysts. *American*  
1018 *Mineralogist* 98, 1779–1787. <https://doi.org/10.2138/am.2013.4521>
- 1019 Jónasson, K., 2007. Silicic volcanism in Iceland: Composition and distribution within the active  
1020 volcanic zones. *Journal of Geodynamics* 43, 101–117. <https://doi.org/10.1016/j.jog.2006.09.004>
- 1021 Kenedi, C., Shalev, E., Lucas, A., Malin, P., 2010. Microseismicity and 3-D Mapping of an Active  
1022 Geothermal Field, Kilauea Lower East Rift Zone, Puna, Hawaii. Presented at the Proceedings World  
1023 Geothermal Congress 2010.
- 1024 Kent, G.M., Singh, S.C., Harding, A.J., Sinha, M.C., Orcutt, J.A., Barton, P.J., White, R.S., Bazin, S.,  
1025 Hobbs, R.W., Tong, C.H., Pye, J.W., 2000. Evidence from three-dimensional seismic reactivity images  
1026 for enhanced melt supply beneath mid-ocean -ridge discontinuities 406, 5.
- 1027 Koleszar, A.M., Saal, A.E., Hauri, E.H., Nagle, A.N., Liang, Y., Kurz, M.D., 2009. The volatile contents of  
1028 the Galapagos plume; evidence for H<sub>2</sub>O and F open system behavior in melt inclusions. *Earth and*  
1029 *Planetary Science Letters* 287, 442–452. <https://doi.org/10.1016/j.epsl.2009.08.029>
- 1030 Lerner, A.H., Wallace, P., Shea, T., 2021. The petrologic and degassing behavior of sulfur and other  
1031 magmatic volatiles from the 2018 eruption of Kīlauea, Hawai'i: melt concentrations, magma storage  
1032 depths, and magma recycling. *Bulletin Volcanology* 83:43, 1–32.
- 1033 Llewellyn, E.W., Mader, H.M., Wilson, S.D.R., 2002. The rheology of a bubbly liquid. *Proc. R. Soc.*  
1034 *Lond. A* 458, 987–1016. <https://doi.org/10.1098/rspa.2001.0924>
- 1035 Lowenstern, J., 2001. Carbon dioxide in magmas and implications for hydrothermal systems.  
1036 *Mineralium Deposita* 36, 490–502. <https://doi.org/10.1007/s001260100185>
- 1037 Macdonald, G.A., 1962. The 1959 and 1960 eruptions of Kilauea volcano, Hawaii, and the  
1038 construction of walls to restrict the spread of the lava flows. *Bull Volcanol* 24, 249–294.  
1039 <https://doi.org/10.1007/BF02599351>

- 1040 Manga, M., Loewenberg, M., 2001. Viscosity of magmas containing highly deformable bubbles.  
1041 Journal of Volcanology and Geothermal Research 105, 19–24. <https://doi.org/10.1016/S0377->  
1042 0273(00)00239-0
- 1043 Marske, J.P., 2010. Magmatic History Of Lavas from Kīlauea Volcano, Hawai'i and South Pagan  
1044 Volcano, Northern Mariana Islands. PhD Thesis, UH Manoa.
- 1045 Masotta, M., Mollo, S., Nazzari, M., Tecchiato, V., Scarlato, P., Papale, P., Bachmann, O., 2018.  
1046 Crystallization and partial melting of rhyolite and felsite rocks at Krafla volcano: A comparative  
1047 approach based on mineral and glass chemistry of natural and experimental products. Chemical  
1048 Geology 483, 603–618. <https://doi.org/10.1016/j.chemgeo.2018.03.031>
- 1049 Mbia, P., Mortensen, A., Oskarsson, N., Hardarson, B., 2015. Sub-surface geology, petrology and  
1050 hydrothermal alteration of the Menengai geothermal field, Kenya: Case study of wells MW-02, MW-  
1051 04, MW-06 and MW-07. Presented at the World Geothermal Congress 2015.  
1052 <https://www.geothermal-energy.org/pdf/IGStandard/WGC/2015/12071.pdf>.
- 1053 Moore, R.B., 1992. Volcanic geology and eruption frequency, lower east rift zone of Kilauea volcano,  
1054 Hawaii. Bulletin of Volcanology 54, 475–483. <https://doi.org/10.1007/BF00301393>
- 1055 Mortensen, A.K., Gronvold, K., Gudmundsson, A., Steingrímsson, B., Egilson, T., 2010. Quenched  
1056 Silicic Glass from Well KJ-39 in Krafla, North-Eastern Iceland, in: Proceedings World Geothermal  
1057 Congress 2010, Bali, Indonesia, 25-29 April 2010.
- 1058 Moussallam, Y., Edmonds, M., Scaillet, B., Peters, N., Gennaro, E., Sides, I., Oppenheimer, C., 2016.  
1059 The impact of degassing on the oxidation state of basaltic magmas: A case study of Kīlauea volcano.  
1060 Earth and Planetary Science Letters 450, 317–325. <https://doi.org/10.1016/j.epsl.2016.06.031>
- 1061 Neal, C.A., Brantley, S.R., Antolik, L., Babb, J.L., Burgess, M., Calles, K., Cappos, M., Chang, J.C.,  
1062 Conway, S., Desmither, L., Dotray, P., Elias, T., Fukunaga, P., Fuke, S., Johanson, I.A., Kamibayashi, K.,  
1063 Kauahikaua, J., Lee, R.L., Pekalib, S., Miklius, A., Million, W., Moniz, C.J., Nadeau, P.A., Okubo, P.,  
1064 Parcheta, C., Patrick, M.R., Shiro, B., Swanson, D.A., Tollett, W., Trusdell, F., Younger, E.F., Zoeller,  
1065 M.H., Montgomery-Brown, E.K., Anderson, K.R., Poland, M.P., Ball, J.L., Bard, J., Coombs, M.,  
1066 Dietterich, H.R., Kern, C., Thelen, W.A., Cervelli, P.F., Orr, T., Houghton, B.F., Gansecki, C., Hazlett, R.,  
1067 Lundgren, P., Diefenbach, A.K., Lerner, A.H., Waite, G., Kelly, P., Clor, L., Werner, C., Mulliken, K.,  
1068 Fisher, G., Damby, D., 2018. The 2018 rift eruption and summit collapse of Kīlauea Volcano. Science  
1069 eaav7046. <https://doi.org/10.1126/science.aav7046>
- 1070 Neave, D.A., Hartley, M.E., Maclennan, J., Edmonds, M., Thordarson, T., 2017. Volatile and light  
1071 lithophile elements in high-anorthite plagioclase-hosted melt inclusions from Iceland. Geochimica et  
1072 Cosmochimica Acta 205, 100–118. <https://doi.org/10.1016/j.gca.2017.02.009>
- 1073 Norman, M., 2005. Trace-element distribution coefficients for pyroxenes, plagioclase, and olivine in  
1074 evolved tholeiites from the 1955 eruption of Kilauea Volcano, Hawai'i, and petrogenesis of  
1075 differentiated rift-zone lavas. American Mineralogist 90, 888–899.  
1076 <https://doi.org/10.2138/am.2005.1780>
- 1077 Parfitt, E.A., Wilson, L., 1995. Explosive volcanic eruptions-IX. The transition between Hawaiian-style  
1078 lava fountaining and Strombolian explosive activity. Geophysical Journal International 121, 226–232.  
1079 <https://doi.org/10.1111/j.1365-246X.1995.tb03523.x>

- 1080 Patrick, M.R., Dietterich, H.R., Lyons, J.J., Diefenbach, A.K., Parcheta, C., Anderson, K.R., Namiki, A.,  
1081 Sumita, I., Shiro, B., Kauahikaua, J.P., 2019. Cyclic lava effusion during the 2018 eruption of Kīlauea  
1082 Volcano. *Science* 366, eaay9070. <https://doi.org/10.1126/science.aay9070>
- 1083 Patrick, M.R., Houghton, B.F., Anderson, K.R., Poland, M.P., Montgomery-Brown, E., Johanson, I.,  
1084 Thelen, W., Elias, T., 2020. The cascading origin of the 2018 Kīlauea eruption and implications for  
1085 future forecasting. *Nat Commun* 11, 5646. <https://doi.org/10.1038/s41467-020-19190-1>
- 1086 Pietruszka, A.J., Garcia, M.O., 1999a. A Rapid Fluctuation in the Mantle Source and Melting History  
1087 of Kilauea Volcano Inferred from the Geochemistry of its Historical Summit Lavas (1790–1982).  
1088 *Journal of Petrology* 40, 1321–1342.
- 1089 Pietruszka, A.J., Garcia, M.O., 1999b. The size and shape of Kilauea Volcano’s summit magma storage  
1090 reservoir: a geochemical probe. *Earth and Planetary Science Letters* 167, 311–320.  
1091 [https://doi.org/10.1016/S0012-821X\(99\)00036-9](https://doi.org/10.1016/S0012-821X(99)00036-9)
- 1092 Pietruszka, A.J., Garcia, M.O., Rhodes, J.M., 2021. Accumulated Pu’u ‘Ō’ō magma fed the voluminous  
1093 2018 rift eruption of Kīlauea Volcano: evidence from lava chemistry. *Bull Volcanol* 83, 59.  
1094 <https://doi.org/10.1007/s00445-021-01470-3>
- 1095 Pietruszka, A.J., Heaton, D.E., Marske, J.P., Garcia, M.O., 2015. Two magma bodies beneath the  
1096 summit of Kīlauea Volcano unveiled by isotopically distinct melt deliveries from the mantle. *Earth  
1097 and Planetary Science Letters* 413, 90–100. <https://doi.org/10.1016/j.epsl.2014.12.040>
- 1098 Portnyagin, M., Almeev, R., Matveev, S., Holtz, F., 2008. Experimental evidence for rapid water  
1099 exchange between melt inclusions in olivine and host magma. *Earth and Planetary Science Letters*  
1100 272, 541–552. <https://doi.org/10.1016/j.epsl.2008.05.020>
- 1101 Rooney, T.O., Hart, W.K., Hall, C.M., Ayalew, D., Ghiorso, M.S., Hidalgo, P., Yirgu, G., 2012.  
1102 Peralkaline magma evolution and the tephra record in the Ethiopian Rift. *Contrib Mineral Petrol* 164,  
1103 407–426. <https://doi.org/10.1007/s00410-012-0744-6>
- 1104 Rooyackers, Shane M, Stix, J., Berlo, K., Petrelli, M., Hampton, R.L., Barker, S.J., Morgavi, D., 2021.  
1105 The Origin of Rhyolitic Magmas at Krafla Central Volcano (Iceland). *Journal of Petrology* 62, egab064.  
1106 <https://doi.org/10.1093/petrology/egab064>
- 1107 Rooyackers, Shane M., Stix, J., Berlo, K., Petrelli, M., Sigmundsson, F., 2021. Eruption risks from  
1108 covert silicic magma bodies. *Geology*. <https://doi.org/10.1130/G48697.1>
- 1109 Russell, J.K., Stanley, C., 1990. Origins of the 1954-1960 Lavas, Kilauea Volcano, Hawaii: Major  
1110 Element Constraints on Shallow Reservoir Magmatic Processes. *Journal of Geophysical Research* 95,  
1111 5021–5047.
- 1112 Sides, Edmonds, M., Maclennan, J., Houghton, B.F., Swanson, D.A., Steele-MacInnis, M.J., 2014a.  
1113 Magma mixing and high fountaining during the 1959 Kīlauea Iki eruption, Hawai’i. *Earth and  
1114 Planetary Science Letters* 400, 102–112. <https://doi.org/10.1016/j.epsl.2014.05.024>
- 1115 Sides, Edmonds, M., Maclennan, J., Swanson, D.A., Houghton, B.F., 2014b. Eruption style at Kīlauea  
1116 Volcano in Hawai’i linked to primary melt composition. *Nature Geoscience* 7, 464–469.  
1117 <https://doi.org/10.1038/ngeo2140>



- 1118 Soldati, A., Houghton, B.F., Dingwell, D.B., 2021. A lower bound on the rheological evolution of  
1119 magmatic liquids during the 2018 Kilauea eruption. *Chemical Geology* 576, 120272.  
1120 <https://doi.org/10.1016/j.chemgeo.2021.120272>
- 1121 Sparks, S.R.J., Sigurdsson, H., Wilson, L., 1977. Magma mixing: a mechanism for triggering acid  
1122 explosive eruptions. *Nature* 267, 315–318. <https://doi.org/10.1038/267315a0>
- 1123 Stock, M.J., Geist, D., Neave, D.A., Gleeson, M.L.M., Bernard, B., Howard, K.A., Buisman, I.,  
1124 Maclennan, J., 2020. Cryptic evolved melts beneath monotonous basaltic shield volcanoes in the  
1125 Galápagos Archipelago. *Nat Commun* 11, 3767. <https://doi.org/10.1038/s41467-020-17590-x>
- 1126 Swanson, D.A., Duffield, W.A., Jackson, D.B., Peterson, D.W., 1979. Chronological narrative of the  
1127 1969–71 Mauna Ulu eruption of Kilauea Volcano, Hawaii. *Geological Survey Professional Paper* 1056.
- 1128 Teplow, W., Marsh, B., Hulen, 2009. Dacite Melt at the Puna Geothermal Venture Wellfield, Big  
1129 Island of Hawaii. *GRC Transactions* 33.
- 1130 Trusdell, F., Wolfe, E., Morris, J., 2006. Digital Database of the Geologic Map of the Island of Hawai'i.  
1131 USGS Data Series 144.
- 1132 Wanless, V.D., Perfit, M.R., Ridley, W.I., Klein, E., 2010. Dacite Petrogenesis on Mid-Ocean Ridges:  
1133 Evidence for Oceanic Crustal Melting and Assimilation. *Journal of Petrology* 51, 2377–2410.  
1134 <https://doi.org/10.1093/petrology/egq056>
- 1135 Wieser, P., Iacovino, K., Matthews, S., Moore, G., Allison, C., in press. VESlcal II - A Critical Approach  
1136 to Volatile Solubility Modelling using an Open-Source Python3 Engine. *Earth and Space Science*,  
1137 preprint at <https://doi.org/10.31223/X5K03T>.
- 1138 Wieser, P.E., Edmonds, M., Maclennan, J., Jenner, F.E., Kunz, B.E., 2019. Crystal Scavenging from  
1139 Mush Piles Recorded by Melt Inclusions. *Nature Communications*.
- 1140 Wieser, P.E., Iacovino, K., Matthews, S., 2021a. VESlcal part II.
- 1141 Wieser, P.E., Jenner, F., Edmonds, M., Maclennan, J., Kunz, B.E., 2020. Chalcophile elements track  
1142 the fate of sulfur at Kilauea Volcano, Hawai'i. *Geochimica et Cosmochimica Acta*  
1143 S0016703720303239. <https://doi.org/10.1016/j.gca.2020.05.018>
- 1144 Wieser, P.E., Lamadrid, H., Maclennan, J., Edmonds, M., Matthews, S., Iacovino, K., Jenner, F.E.,  
1145 Gansecki, C., Trusdell, F., Lee, R.L., Ilyinskaya, E., 2021b. Reconstructing Magma Storage Depths for  
1146 the 2018 Kilauean Eruption From Melt Inclusion CO<sub>2</sub> Contents: The Importance of Vapor Bubbles.  
1147 *Geochem Geophys Geosyst* 22. <https://doi.org/10.1029/2020GC009364>
- 1148 Wilson, L., Head, J.W., 1981. Ascent and eruption of basaltic magma on the Earth and Moon. *J.*  
1149 *Geophys. Res.* 86, 2971–3001. <https://doi.org/10.1029/JB086iB04p02971>
- 1150 Wright, T.L., Fiske, R.S., 1971. Origin of the Differentiated and Hybrid Lavas of Kilauea Volcano,  
1151 Hawaii. *Journal of Petrology* 12, 1–65. <https://doi.org/10.1093/petrology/12.1.1>
- 1152 Wright, T.L., Peck, D.L., Shaw, H.R., 1976. Kilauea Lava Lakes: Natural Laboratories for Study of  
1153 Cooling, Crystallization, and Differentiation of Basaltic Magma, in: Sutton, G.H., Manghnani, M.H.,  
1154 Moberly, R., Mcafee, E.U. (Eds.), *Geophysical Monograph Series*. American Geophysical Union,  
1155 Washington, D. C., pp. 375–390. <https://doi.org/10.1029/GM019p0375>

**This was a preprint submitted to EarthArxiv.**

**PLEASE REFER TO THE PUBLISHED VERSION OF THE ARTICLE, AVAILABLE OPEN-ACCESS AT:  
<https://doi.org/10.1029/2021GC010046>, WHICH HAS SOME TYPOS CORRECTED AND NICER  
FORMATTING**

1156 Zoeller, M.H., Perroy, R.L., Wessels, R., Fisher, G.B., Robinson, J.E., Bard, J.A., Peters, J., Mosbrucker,  
1157 A., Parcheta, C.E., 2020. Geospatial database of the 2018 lower East Rift Zone eruption of Kilauea  
1158 Volcano, Hawaii. <https://doi.org/10.5066/P9S7UQKQ>

1159